

Electronic Supplementary Information for

New monoclinic ruthenium dioxide with highly selective hydrogenation activity

Hee Jung Yang,^a Morgan Redington,^b Daniel P. Miller,^c Eva Zurek,^{*,b} Minseob Kim,^d Choong-Shik Yoo,^d Soo Yeon Lim,^e Hyeonsik Cheong,^e Seen-Ae Chae,^f Docheon Ahn,^g Nam Hwi Hur^{*,a}

^aDepartment of Chemistry, Sogang University, Seoul 04107, Korea

^bDepartment of Chemistry, State University of New York at Buffalo, Buffalo, NY 14260, USA

^cDepartment of Chemistry, Hofstra University, Hempstead, NY 11549, USA

^dDepartment of Chemistry, Institute for Shock Physics, Washington State University, Pullman, WA 99164, USA

^eDepartment of Physics, Sogang University, Seoul 04107, Korea

^fWestern Seoul Center, Korea Basic Science Institute, Seoul 03759, Korea

^gBeamline Research Division, Pohang Accelerator Laboratory, Pohang University of Science and Technology, Pohang 37673, Korea

*Electronic mails: nhhur@sogang.ac.kr, ezurek@buffalo.edu

Table of Contents

- I. Supplementary methods**
- II. Supplementary figures**
- III. Supplementary tables**
- IV. Supplementary computational information (SCI)**
- V. Supplementary references**
- VI. Supplementary data**

I. Supplementary methods

General. All the chemicals were obtained from commercial suppliers and used without further purification unless otherwise stated. Anhydrous ruthenium dioxide (RuO_2) was purchased from Pressure Chemical Co. Hydrous ruthenium dioxide ($\text{RuO}_2 \cdot x\text{H}_2\text{O}$), 5 wt% $\text{Ru}@\text{Al}_2\text{O}_3$, and cyclohexane (99.9 %) were purchased from Sigma-Aldrich (St. Louis, MO, USA). Toluene (99.9 %) was purchased from Daejung Chemicals (Seoul, Korea). 9-Ethylcarbazole (99 %) was purchased from Thermo Fisher Scientific (Boston, USA). H_2 (99.9%) and CO (99.95%) gases were purchased from Donga Industrial Gas (Seoul, Korea). CDCl_3 (99.8 %) was obtained from Cambridge Isotope (Cambridge, UK). All organic products were characterized by ^1H and ^{13}C NMR. ^1H and ^{13}C NMR spectra were recorded on a Varian 400-MHz Gemini. The ^1H and ^{13}C NMR chemical shifts were referenced to the center of solvent resonance (CDCl_3 : 7.26 ppm (^1H), 77.16 ppm (^{13}C)).

Catalytic hydrogenation of benzene using deuterium labeling D_xRuO_2 catalyst. The catalytic hydrogenation of benzene with D_xRuO_2 was conducted in a 45 mL stainless autoclave. Benzene (0.3 mL) was mixed with the D_xRuO_2 catalyst (10 mg) in a 10 mL reaction vial equipped with a magnetic stirring bar. The reaction vial was placed into the autoclave. The autoclave was purged twice with H_2 at room temperature, which was then pressurized with H_2 to 1 MPa. The autoclave was maintained at 50 °C with stirring for 30 min. After completion of the reaction, the autoclave was cooled to room temperature. The products were analyzed by gas chromatography-mass spectrometer. Deuterium substituted cyclohexane is included in the product. The peaks of $m/z = 84$, $m/z = 90$, and $m/z = 93$ were detected, which correspond to $\text{C}_6\text{H}_{12}^+$, $\text{C}_6\text{H}_6\text{D}_6^+$, and $\text{C}_6\text{H}_3\text{D}_9^+$, respectively. In addition, peaks with m/z of 84-96 were detected due to H/D exchange.

Catalyst characterization. Powder XRD patterns were recorded with a Rigaku DMAX 2500 diffractometer (Cu $-\text{K}\alpha$, Tokyo, Japan) operating at 40 kV and 15 mA. High-resolution synchrotron powder X-ray diffraction data of the samples were measured at 9B beamline of PLS-II. The incident X-rays ($20 \times 1 \text{ mm}^2$ beam size at the sample position) were vertically collimated by a mirror, and monochromatized to the wavelength of 1.52120 (1) Å using a double-crystal Si(111) monochromator. The detector arm of the vertical scan diffractometer is composed of seven sets of soller slits, flat Ge (111) crystal analyzers, anti-scatter baffles, and scintillation detectors, with each set separated by 20 degrees. Each specimen of approximately 0.2 g of powder was prepared by flat plate side loading method to avoid the preferred orientation, and the sample was then rotated about the normal to the surface during the measurement to increase sampling statistics. A step scan was performed at room temperature from 10° in 2θ with 0.01° increments and 1° overlaps to the next detector bank up to 130.5° in 2θ . Thermogravimetric analysis was conducted

using a TGA 2050 instrument (TA Instruments, USA). Samples were placed on a platinum pan and analyzed under nitrogen from 30 to 800 °C at a heating rate of 5 °C/min. Differential scanning calorimetry (DSC) experiments were performed using a DSC Q-2000 instrument (TA Instruments, USA). All scans were carried out at a heating rate of 20 °C/min under nitrogen. The temperature-programmed desorption (TPD) experiments were carried out using a BELCAT-B, BEL JAPAN Inc. The sample was annealed with argon from room temperature to 80 °C at a heating rate of 5 °C/min and further kept at 80 °C for 1 hr. The desorption was carried out by heating the samples at a rate of 5 °C/min from 50 °C to 400 °C. The outlet gas was analyzed by a benchtop-type quadrupole mass spectrometer (BELMass). The Fourier transform infrared (FT-IR) spectra were measured on a Nicolet 205 FT-IR spectrometer in ATR modes, scanning from 4000 to 600 cm^{-1} at room temperature. To investigate the elemental compositions, X-ray photoelectron spectroscopy (XPS; Theta probe AR-XPS System, Thermo Fisher Scientific, UK) analysis was conducted using a monochromated Al $K\alpha$ X-ray source ($h\nu = 1486.6 \text{ eV}$) at the Korea Basic Science Institute (KBSI). The ^1H magic angle spinning (MAS) nuclear magnetic resonance (NMR) spectra were acquired on a Unity INOVA 600 NMR spectrometer (Varian Inc.) using a 2.5 mm rotor spinning at a rate of 23 kHz. We performed Raman spectroscopy measurements with a diode-pumped solid-state laser with a wavelength of 514.4 nm (2.41 eV) and the 514.5 nm (2.41 eV) line of an Ar^+ laser. A 50 \times (N.A. = 0.8) and a 40 \times objective lens (N.A. = 0.6) were used to focus the laser to a spot of about 1 μm in diameter with a power of 100 μW and to collect the scattered light from the samples. The scattered light from the samples was dispersed with a Jobin-Yvon Horiba iHR550 spectrometer (2400 grooves per mm) and was detected with a charge-coupled-device (CCD) using liquid nitrogen for cooling. Reflective volume Bragg gratings (OptiGrate) were used as notch filters to remove the Rayleigh scattered signal, which enables us to observe Stokes and anti-Stokes Raman bands down to 5 cm^{-1} . Adsorption and desorption measurements were carried out using an ASAP 2420 instrument (Micromeritics, Norcross, GA, USA), with nitrogen as the adsorptive, at 77 K. The Brunauer-Emmett-Teller (BET) surface areas were calculated using $P/P_0 = 0.05\text{--}0.3$ in the adsorption curve using the BET equation. To investigate the oxidation state of Ru, X-ray photoelectron spectroscopy (XPS; High performance XPS System, Thermo Fisher Scientific, UK) analysis using a mono-chromated Al $K\alpha$ X-ray source ($h\nu=1486.6 \text{ eV}$) was performed at the Korea Basic Science Institute (KBSI) in Busan. The surface morphology was studied by scanning electron microscopy (SEM). High-resolution scanning electron microscopy analyses were carried out using a Hitachi S-5500 microscope (Hitachi, Japan).

Gas chromatography-mass spectrometry

Products were analyzed using an Agilent 6890N gas chromatograph interfaced to an Agilent 5975C mass-selective detector (70 eV, electron ionization source). The mass spectra were scanned in the mass range 50-650 u. A dimethylpolysiloxane based GC capillary column (Agilent HP-5MS)

was used. The injector and the detector temperatures were set at 523 K. A temperature program for the analysis of hydrogenation products was employed for analysis starting at 323 K, holding for 3 min, followed by a 25 K min⁻¹ program rate to 100 K.

II. Supplementary figures

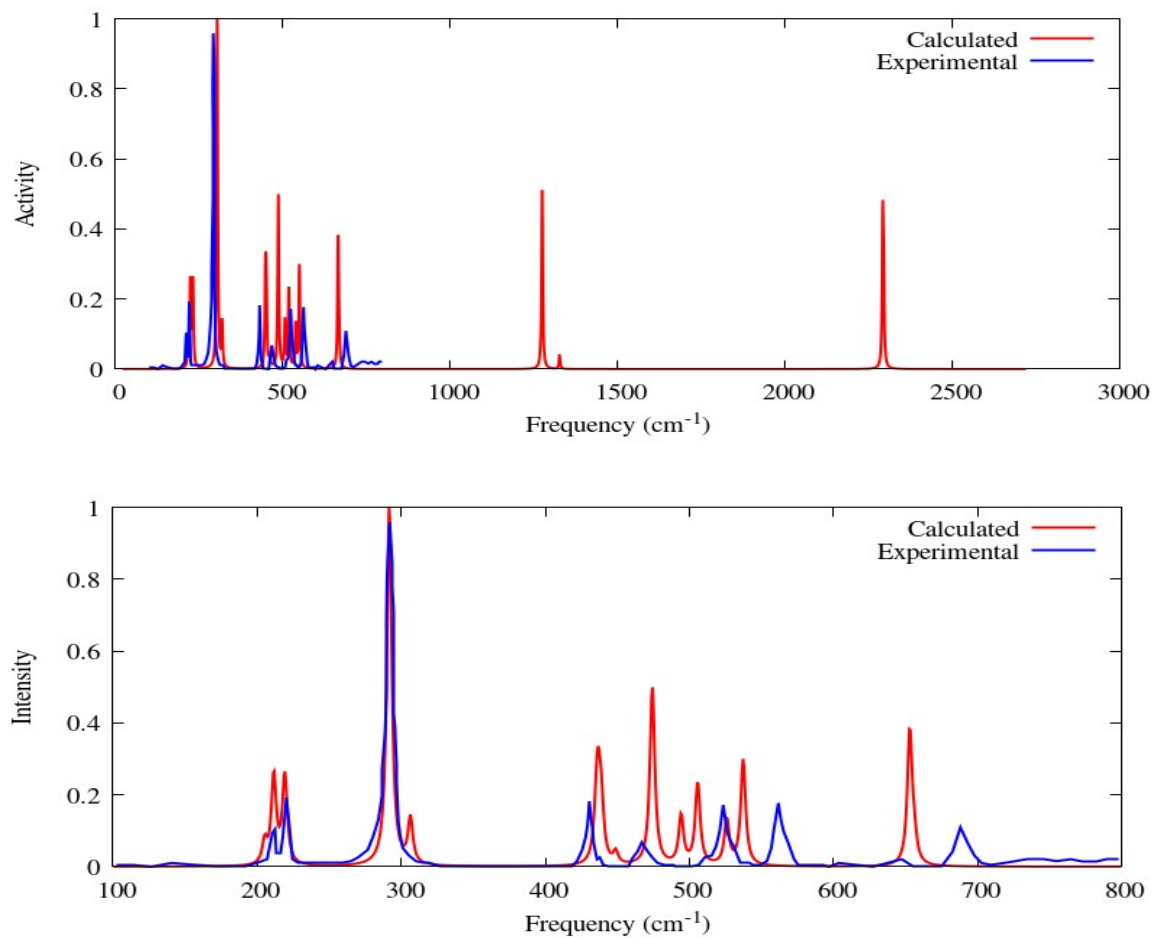


Fig. S1 Calculated Raman spectra vs experimental Raman spectra from 0-3,000 cm⁻¹ (upper). A plot of the lower wavenumber peaks is also shown for ease of comparison (lower). Frequencies were shifted by 41 cm⁻¹ to establish best fit with low wavenumber peak positions, and a Gaussian broadening was applied with a variance of 10 cm⁻¹.

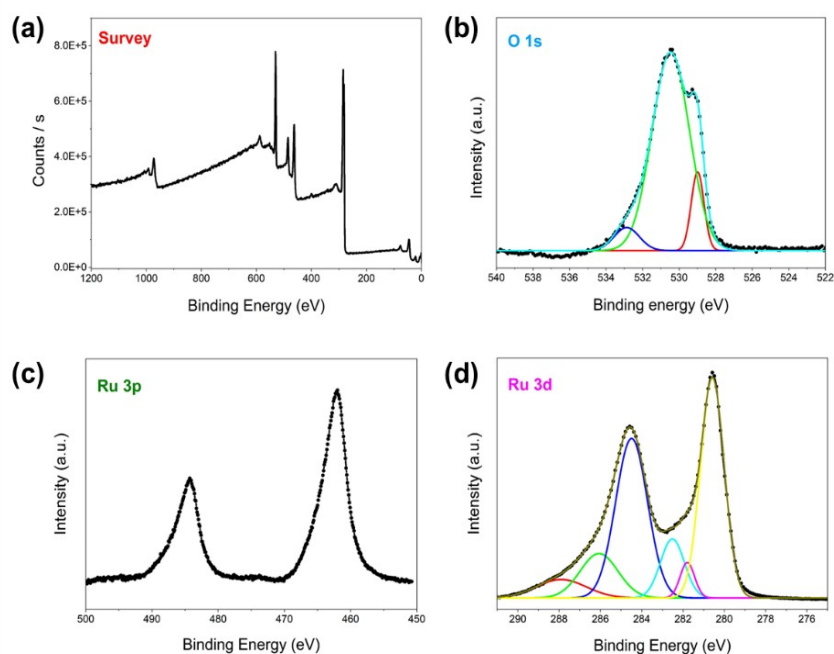


Fig. S2 XPS spectra of H_xRuO_2 powders: (a) low resolution XPS survey spectrum, (b) high-resolution O 1s XPS spectrum, (c) high-resolution Ru 3p XPS spectrum, and (d) high-resolution Ru 3d XPS spectrum. Fitted spectra are described as follows: In (b), blue, green, and red curves are assigned to physisorbed water, surface hydroxide, and oxygen in RuO_2 lattice, respectively. In (d), yellow, cyan, blue, and green curves are assigned to $Ru\ 3d_{5/2}$, $Ru\ 3d_{5/2}$ satellite peak, $Ru\ 3d_{3/2}$, and $Ru\ 3d_{3/2}$ satellite peak of RuO_2 , respectively. The remaining peaks are assigned to Ru^{3+} species.

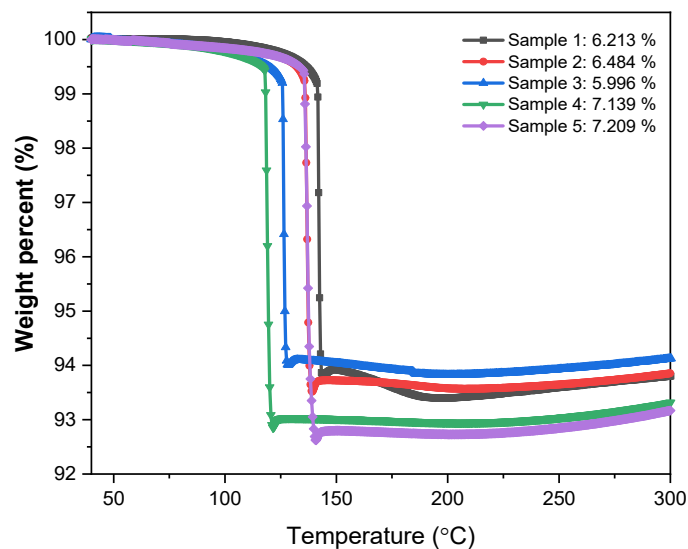


Fig. S3 TGA-curves of five H_xRuO_2 samples synthesized under the same conditions.

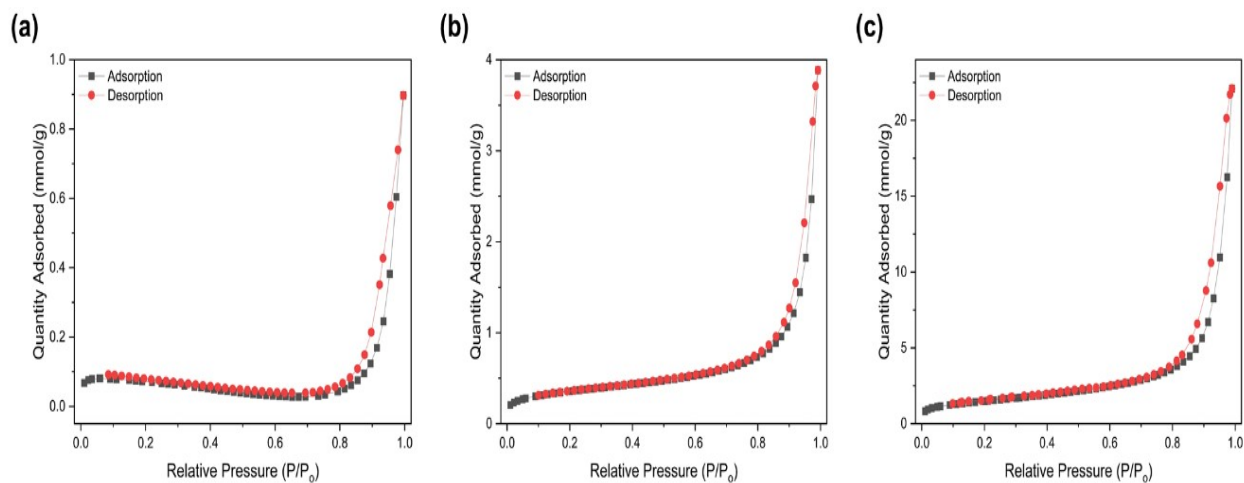


Fig. S4 Nitrogen adsorption and desorption isotherms of (a) rutile RuO_2 , (b) H_xRuO_2 , and (c) 5 wt% $Ru@Al_2O_3$.

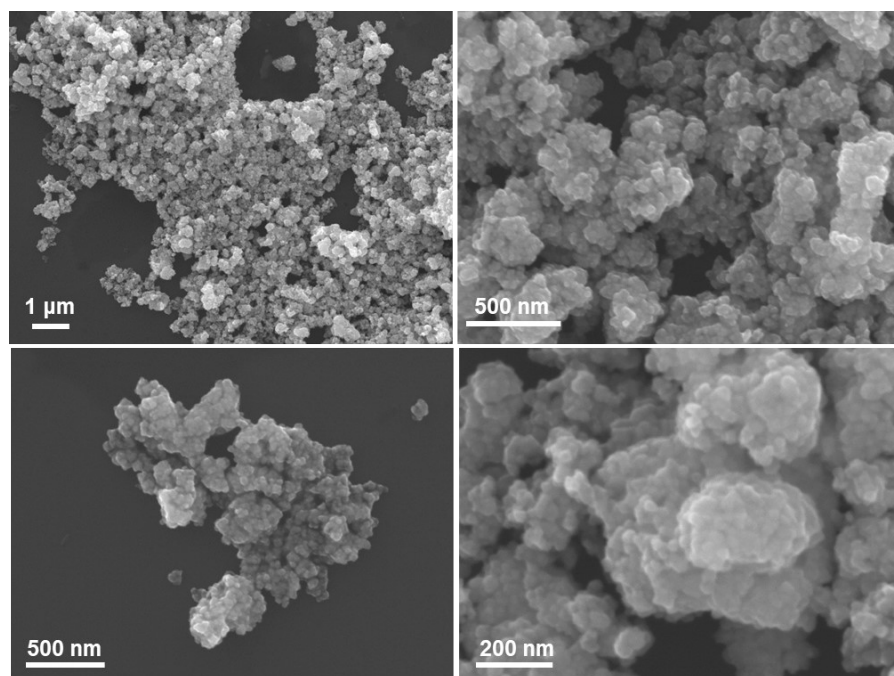


Fig. S5 Scanning electron microscopy (SEM) images of H_xRuO₂ at different magnifications.

III. Supplementary tables

Table S1. Crystallographic data and structure refinement of H_xRuO_2 .

Formula	$Ru_4O_8H_{3.92}$
Radiation	1.52120 Å
2 θ range (deg.)	10-130
<i>T</i> /K	298
Symmetry	Monoclinic
Space group	P 2 ₁ /c
<i>a</i> /Å	5.35232(7)
<i>b</i> /Å	5.06977(2)
<i>c</i> /Å	5.35931(2)
α (deg.)	90
β (deg.)	116.115(3)
γ (deg.)	90
Volume/Å ³	130.579(2)
<i>Z</i>	4
<i>wR</i>	8.716 %
χ^2	4.05

Atoms coordinates

	site	x	y	z	Occ.
Ru1	4e	0.72410	-0.00580	0.22030	1.00
O1	4e	0.64320	0.64190	0.33980	1.00
O2	4e	0.13520	0.85960	0.37670	1.00
H1	4e	0.71430	0.01890	0.70110	0.49
H2	4e	0.50570	0.28899	0.49430	0.49

Table S2. Selected interatomic distances and angles for H_xRuO_2 .

Selected bond length (Å)			
Ru – Ru	2.519	O – Ru	2.148
Ru – Ru	3.149	H1 – O	1.269
O – Ru	1.993	H1 – O	1.224
O – Ru	2.008	H2 – O	1.474
O – Ru	2.011	H2 – O	1.772
O – Ru	2.086	H2 – O	1.889
O – Ru	2.094	H2 – Ru	1.635

Table S4. Hydrogenation of various nitroarenes to aminoarenes catalyzed by H_xRuO_2 .

Entry ^a	Substrate	Product	Temperature [°C]	Pressure [MPa]	Time [h]	Conv. [%]	Selec. [%]
1			45	0.5	1.0	>99	>98
2			45	0.5	1.0	>99	>98
3			55	0.5	1.0	>99	>99
4			55	0.5	1.0	>99	>98
5			40	0.5	1.0	>99	>99
6			40	0.5	1.0	>99	>99

^aReaction condition: batch reaction, substrate (1 mmol), catalyst (10 mg), methanol/H₂O(1:1) 2mL, reaction mixture stirred at 600 r.p.m.

IV. Supplementary computational information (SCI)

1. Computational details

Exploratory crystal structure prediction (CSP) searches using the XTALOPT^{7,8} evolutionary algorithm (EA) 11th release⁹ were carried out to identify the hydrogen content in the synthesized phases. EA runs were performed for the following stoichiometries: RuO_2H_n ($n = 1, 2$) for 1-4, and 8 formula units. The searches used tolerances of 3.0 Å – 12.0 Å for the a , b , and c lattice vectors, while the α , β , and γ angles ranged from 60.0° to 120.0°. Experimental results suggested the system had a volume of ~ 260 Å³ with 8 formula units. Therefore, the expected volume range when analyzing the results was 32.5 ± 5.0 Å³ per formula unit. For RuO_2H_2 , the most enthalpically favored structure had a volume of 42 Å³ per formula unit, whereas for RuO_2H the most enthalpically favored structure had a volume of 32 Å³ per formula unit. In addition, comparison of the X-ray diffraction (XRD) patterns computed for theoretically predicted RuO_2H and RuO_2H_2 structures showed the former was in better agreement with experiment than the latter. Based on these CSP searches and XRD patterns, we concluded that the RuO_2H stoichiometry was likely synthesized in experiments.

With the RuO_2H stoichiometry as our deduced composition, we searched for the synthesized structure using a number of different strategies: (i) CSP searches using structural criteria derived from experimental results, (ii) generating and optimizing structures derived from experimentally obtained XRD patterns, and (iii) employing first principles molecular dynamics (FPMD) simulations on supercells of the most stable $Pmn2_1$ RuO_2H phase found in the EA search.

The FPMD simulations were performed using a canonical (NVT) ensemble with periodic boundary conditions. A $2 \times 2 \times 2$ supercell of a modified $Pmn2_1$ structure (32 formula units total) was used to explore the potential energy landscape. This FPMD simulation ran for 5 ps at 298 K, and a $P2_1/c$ structure based off of the average atomic positions was identified and optimized to the nearest local minimum at 0 K. A second FPMD simulation was run on a $2 \times 2 \times 2$ supercell of the $P2_1/c$ structure (32 formula units total) at 298 K. Further FPMD simulations were run on two model systems that explored the dynamic behavior of hydrogen atoms placed at the partially occupied (POCC) positions deduced from the XRD refined structure (denoted as H1 and H2). The structures were constructed by generating a $2 \times 2 \times 2$ supercell of the $P2_1/c$ structure (32 formula units total), removing four hydrogens from a particular $\text{Ru}_4\text{O}_8\text{H}_4$ unit within it, and adding two hydrogen atoms either at the H1 or at the H2 positions. This procedure yielded a stoichiometry of $\text{RuO}_2\text{H}_{0.9375}$. FPMD simulations were performed on these systems at 298 K for 10 ps.

Precise geometry optimizations, ¹H NMR chemical shifts, electronic density of states, band structure, FPMD, and nudged elastic band (NEB)¹⁰ calculations were performed using density functional theory (DFT) calculations with the Perdew-Burke-Ernzerhof (PBE) functional¹¹ as

implemented in the Vienna *Ab Initio* Simulation Package (VASP)^{12,13}. We employed a plane wave basis set with an energy cutoff of 600 eV, along with projector-augmented wave (PAW) potentials¹⁴ where the H $1s^1$, O $2s^22p^4$, and Ru $4d^75s^1$ electrons were treated explicitly in all calculations. For non-FPMD calculations the k -meshes were generated using the Γ -centered Monkhorst-Pack scheme¹⁵, and the number of divisions along each reciprocal lattice vector was chosen such that the product of this number with the real lattice constant was 50 Å. All FPMD simulations employed the Nose-Hoover thermostat, and due to the size of the cell only sampled the Γ point. ^1H NMR chemical shifts (δ) were calculated in reference to tetramethylsilane (TMS), $\text{Si}(\text{CH}_3)_4$. The unit cell dimensions were kept fixed in all calculations involving the NEB method. The climbing image method, as implemented in VASP, for NEB calculations was used to obtain maxima and intermediates along the minimum energy paths for proton transfers in RuO_2H . All NEB calculations performed were set to produce five images between the select O-H...O hydrogen bonding protons transferring into O...H-O hydrogen bonding positions.

To determine if the predicted structures were dynamically stable, and obtain their zero-point energy, phonons were calculated using the supercell approach. In the supercell approach, Hellmann-Feynman forces were calculated from a supercell constructed by replicating the optimized structure wherein the atoms had been displaced, and dynamical matrices were computed using the PHONOPY¹⁶ code.

Raman spectra were calculated using density functional perturbation theory in combination with VASP. The Raman intensities were evaluated by calculating the derivative of the polarizability (or macroscopic dielectric tensor) with respect to the normal mode eigenvectors¹⁷, as is implemented in the Python program `vasp_raman.py`¹⁸.

2. Predicted RuO_2H structure

Performing FPMD calculations on a supercell of a $Pmn2_1$ structure obtained from the EA resulted in the generation of an average structure with a $P2_1/c$ space group, which maintained the same symmetry after full structural relaxation. The $P2_1/c$ phase possessed a motif of alternating hydrogen bonds along channels, as seen below in Fig. S6, with the second nearest oxygen atom at a distance of 1.26 Å, well within the hydrogen bonding distance. In addition, the $P2_1/c$ phase possessed the lowest enthalpy of any of the structures considered, and its XRD pattern (Fig. S7) was in excellent agreement with experiment.

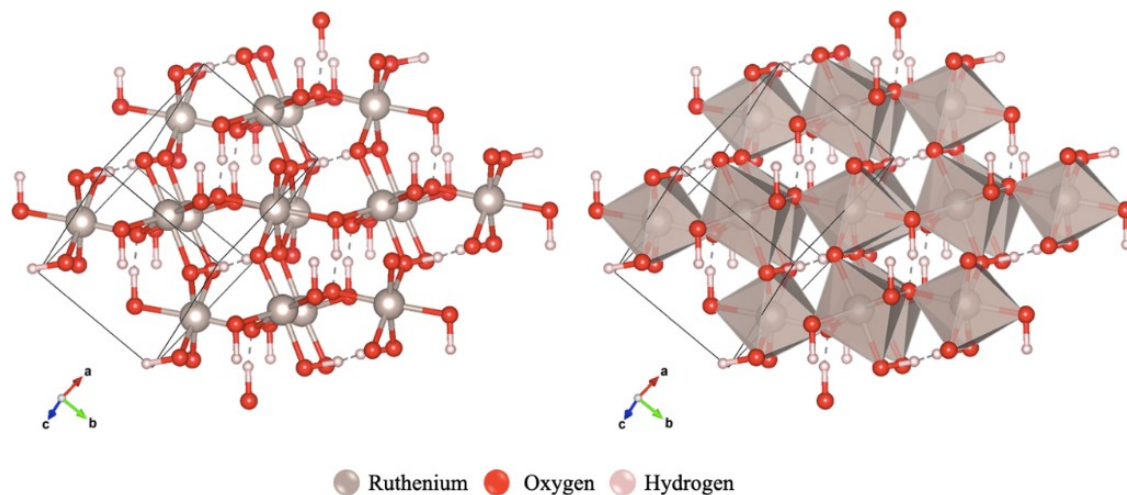


Fig. S6 Predicted $P2_1/c$ structure. Left: Ball and stick model. Right: Ball and stick model with imposed octahedra.

3. Structural parameters and energies

Table S5. Structural parameters for the predicted RuO_2H system

RuO ₂ H, $P2_1/c$ (Z=4) for primitive cell			
a, b, c (Å)	5.4512	5.1271	5.4375
α, β, γ	90.000	116.508	90.000
H(4e)	0.7743	0.0189	0.7142
O(4e)	0.6432	0.6419	0.3398
O(4e)	0.1352	0.8596	0.3767
Ru(4e)	0.7241	-0.0058	0.2203

Table S6. Energies of considered structures for the RuO_2H system

Structure	Space Group	Energy/atom (eV)	Relative energy/atom (eV)	ZPE/atom (eV)	Relative energy/atom with ZPE (eV)
Optimized EA structure	$Pmn2_1$	-6.4667	+0.024	0.123	+0.017
MD average structure	$P2_1/c$	-6.4911	0	0.131	0

4. Computed X-ray diffraction patterns

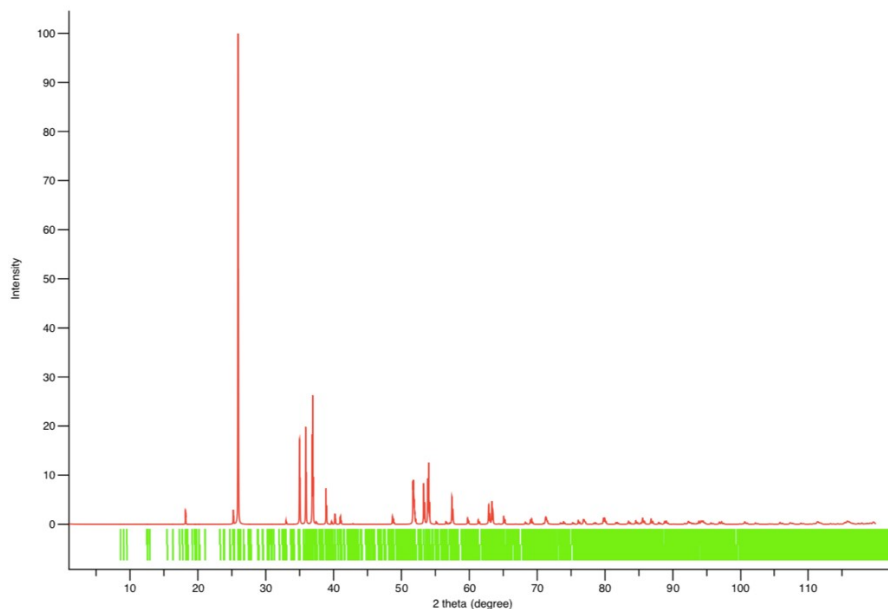


Fig. S7 Computed X-ray diffraction pattern of RuO₂H, P₂₁/c phase. Wavelengths of 1.54059 Å and 1.54432 Å were used with relative intensities of 1 and 0.5, respectively.

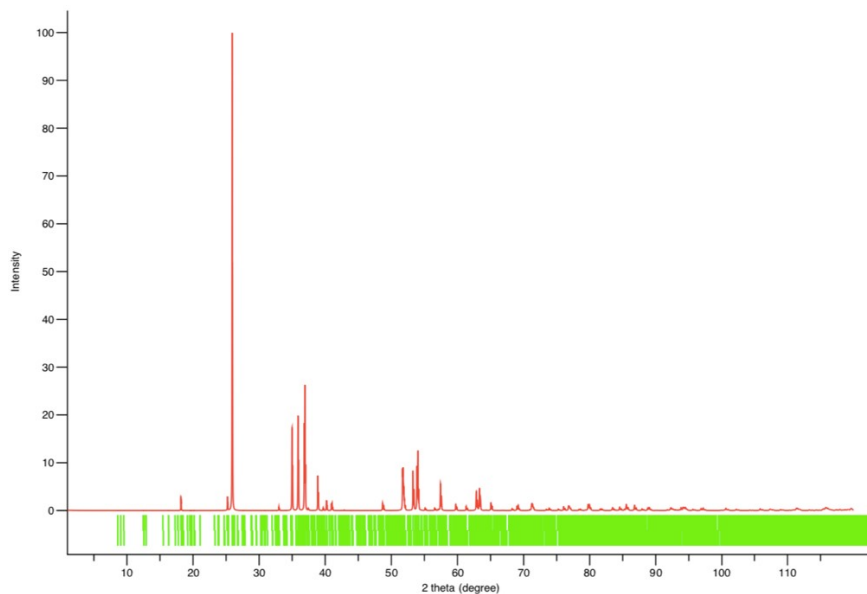


Fig. S8 Computed X-ray diffraction pattern of RuO₂H_{0.9375} H1 POCC supercell structure. Wavelengths of 1.54059 Å and 1.54432 Å were used with relative intensities of 1 and 0.5, respectively.

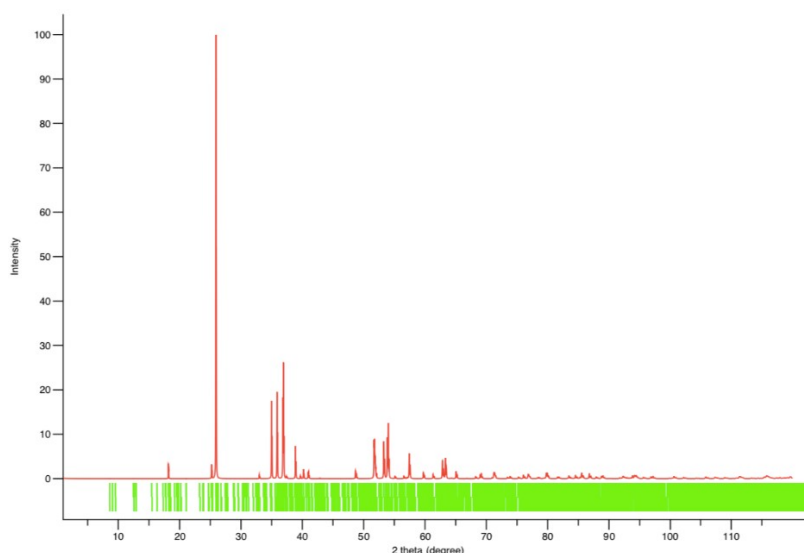


Fig. S9 Computed X-ray diffraction pattern of $\text{RuO}_2\text{H}_{0.9375}$ H₂ POCC supercell structure. Wavelengths of 1.54059 Å and 1.54432 Å were used with relative intensities of 1 and 0.5, respectively.

5. Nudged elastic band proton transfers

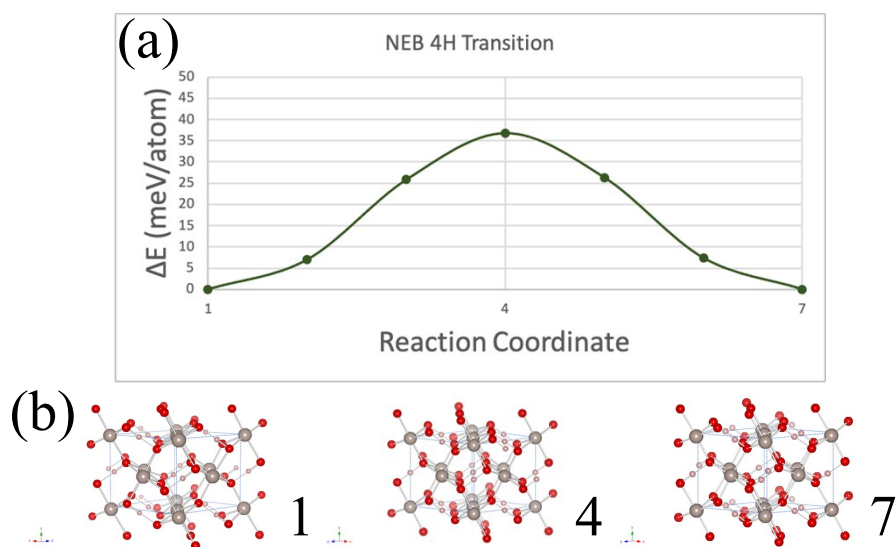


Fig. S10 NEB calculation for the simultaneous transfer of 4 hydrogen atoms (4H) in the conventional $1 \times 1 \times 1$ $P2_1/c$ RuO_2H cell. (a) Relative energy profile for the transition. (b) Structures of RuO_2H that display the position of the hydrogens during the transition, which correspond to the labeled structures along the reaction coordinate and their associated relative energies displayed in (a).

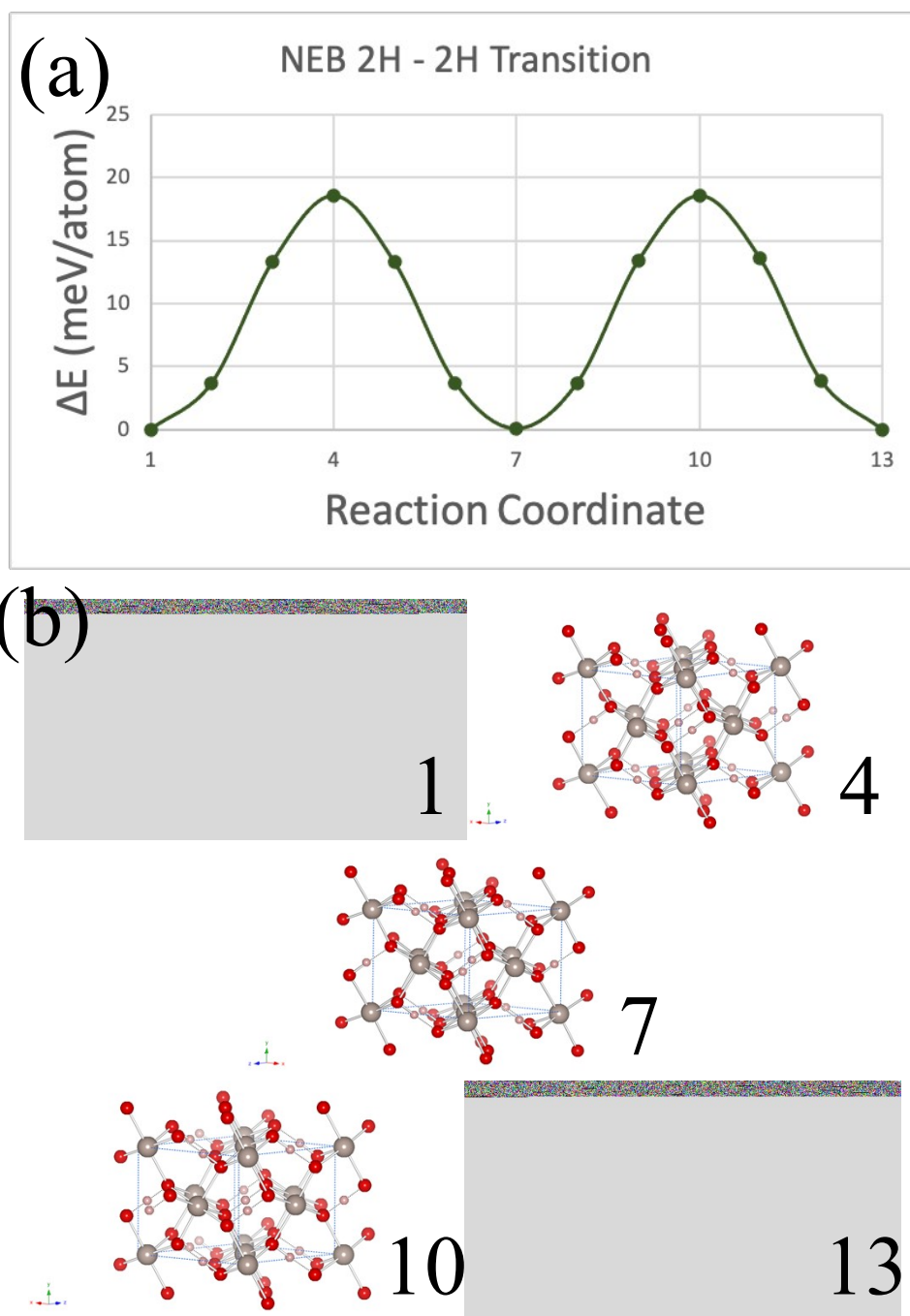


Fig. S11 NEB calculation for the concerted transfer of 2 hydrogen atoms (2H), followed by the transfer of an additional 2 hydrogen atoms in a conventional $1 \times 1 \times 1$ $P2_1/c$ RuO_2H cell. (a) Relative energy profile for the transition. (b) Structures of RuO_2H that display the position of the hydrogens during the transition, which correspond to the labeled structures along the reaction coordinate and their associated relative energies displayed in (a).

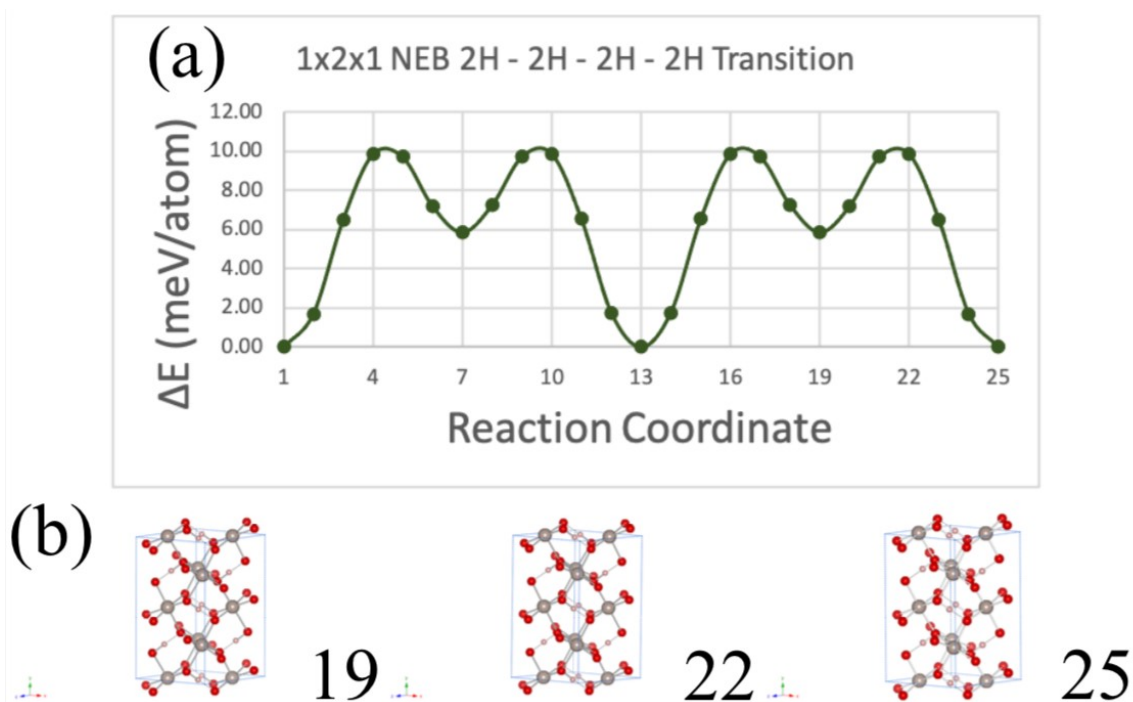


Fig. S12 NEB calculation for the concerted transfer of 2 hydrogen atoms (2H) followed by the transfer of an additional 2 hydrogen atoms occurring twice in 1x2x1 $P2_1/c$ RuO₂H structure. (a) Relative energy profile for the transition. (b) Crystal structures for RuO₂H that display the position of the hydrogens during the transition, which correspond to reaction coordinate structures and their associated relative energies displayed in (a). The structure of the intermediate [19], maxima [22], and ground state images [25] are given, with these structures being similar in energy and topology about the hydrogen atoms to other structures found along the reaction profile, differing only in the identity of the hydrogens that are being transferred.

6. Computed Raman spectra

Computed Raman spectra of RuO₂ rutile ($P4_2/mnm$) structure

To benchmark the computational methodology employed we calculated the Raman spectra of RuO₂ for the rutile structure ($P4_2/mnm$ spacegroup). These results were compared to experimental spectra^{19,20}, with a calibrated comparison presented in Fig. S13. While the relative intensities of the peaks found differed from experiments, the peak positions were in good agreement, with computational results underestimating the experimental results by 41 cm⁻¹. Applying this shift to the computational data yielded good agreement between experimental and computational results, with assigned symmetries in agreement.

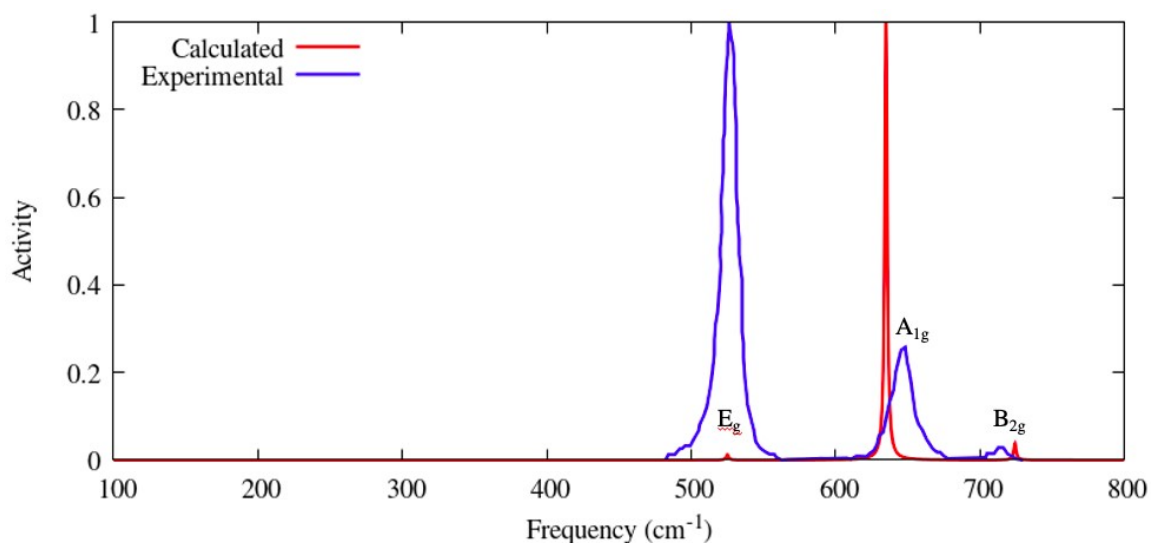


Fig. S13 Calibration of Raman spectrum of the RuO₂ rutile ($P4_2/mnm$) phase. Data points in blue are taken from a previous experimental study^{13,14}, while data points presented in red are taken from this computational study. A Gaussian broadening was applied to the computed data with a variance of 6 cm⁻¹.

Computed Raman spectra of RuO₂H 4H maximum energy phase

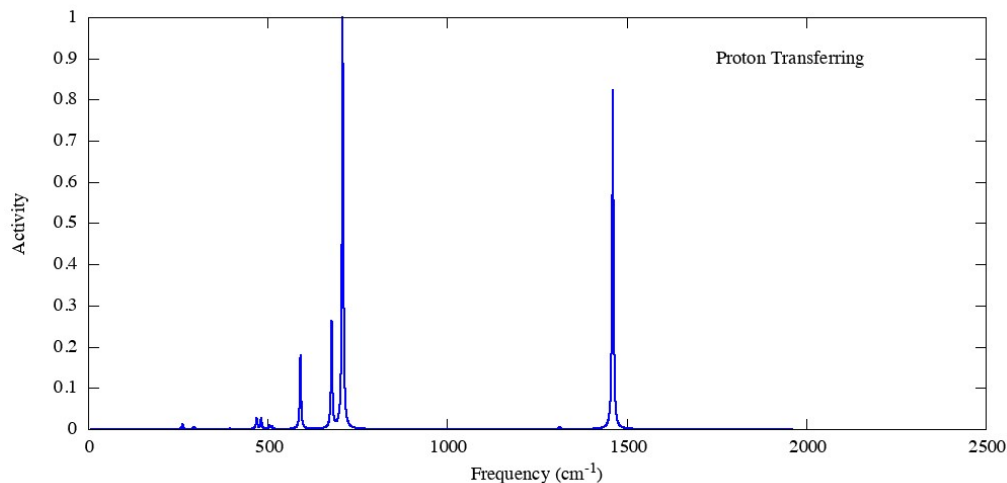


Fig. S14 Calculated Raman spectra for a structure where all of the hydrogen atoms are undergoing proton transfer (maximum in the 4H structure above). Frequencies were shifted by 41 cm⁻¹, as determined via the calibration on the $P2_1/c$ RuO₂H structure, and a Gaussian broadening was applied with a variance of 10 cm⁻¹.

7. Electronic band structure and projected density of states, phonon band structure and density of states

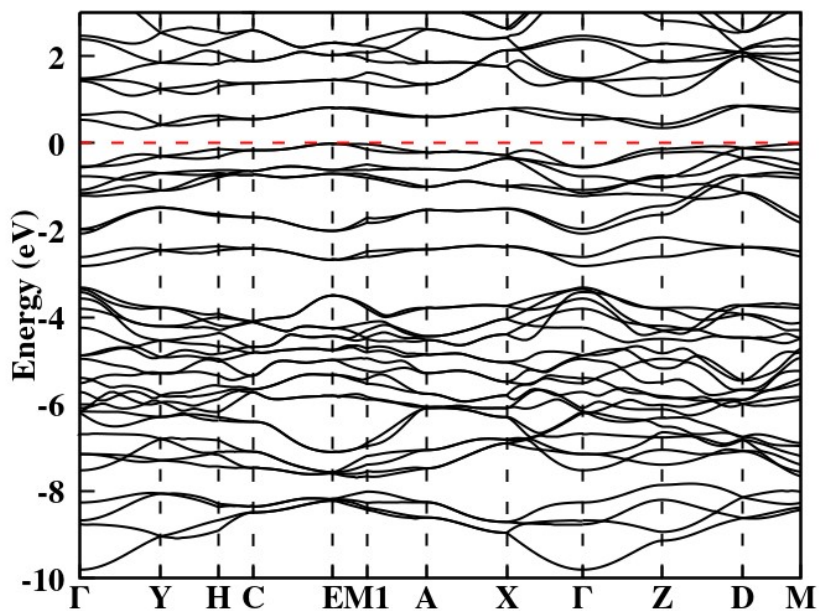


Fig. S15 The electronic band structure of RuO₂H, *P*₂/c phase. The top of the valence band is set to 0 eV.

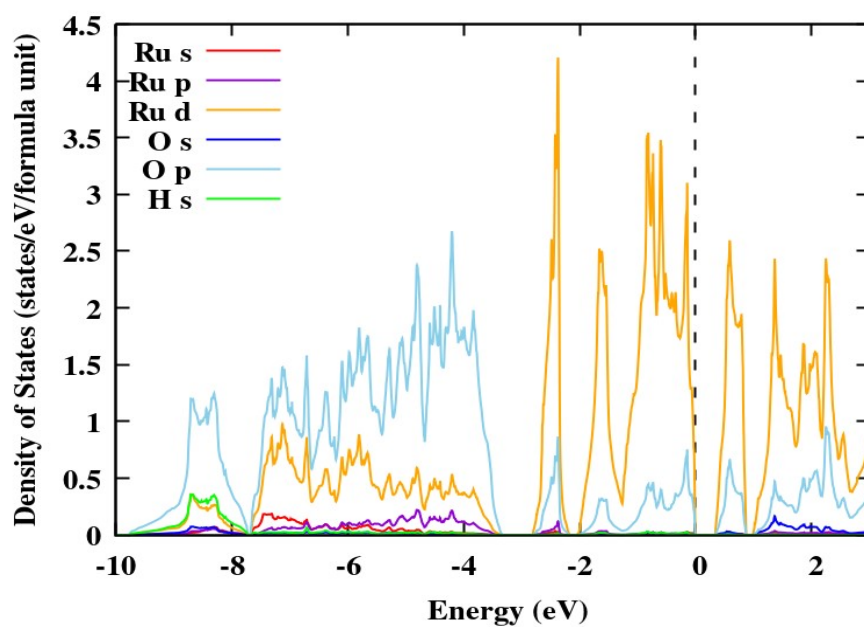


Fig. S16 Electronic projected density of states of RuO_2H , $P2_1/c$ phase. The top of the valence band is set to 0 eV.

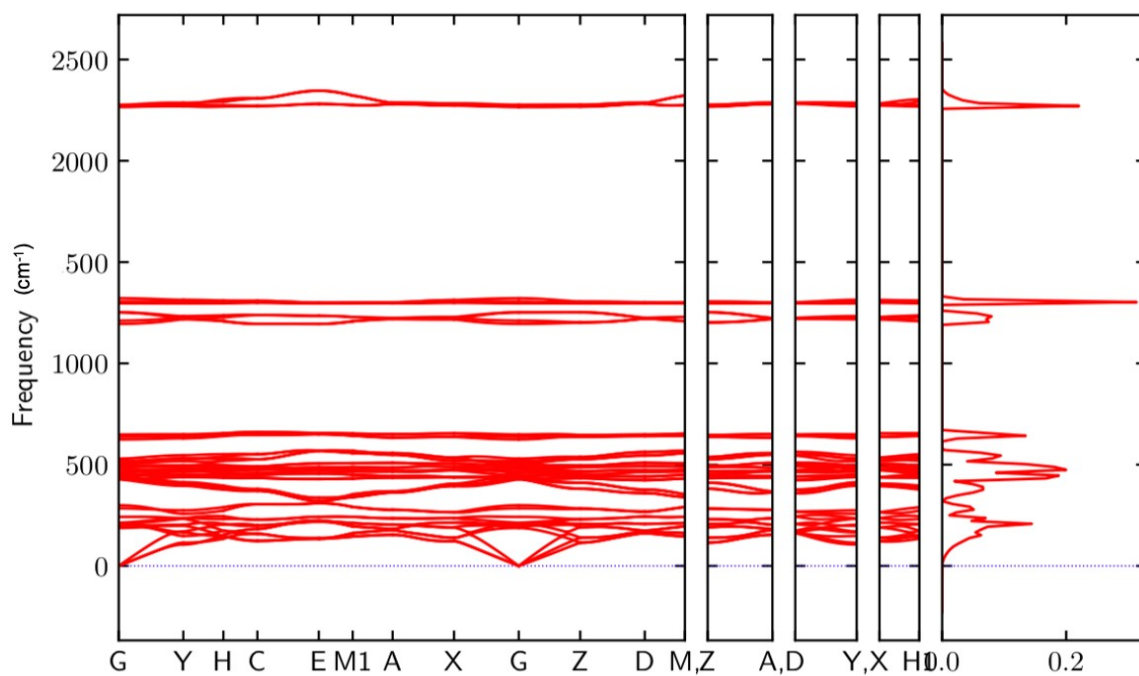


Fig. S17 Phonon band structure and phonon density of states of RuO_2H , $P2_1/c$ phase.

8. First principles molecular dynamics

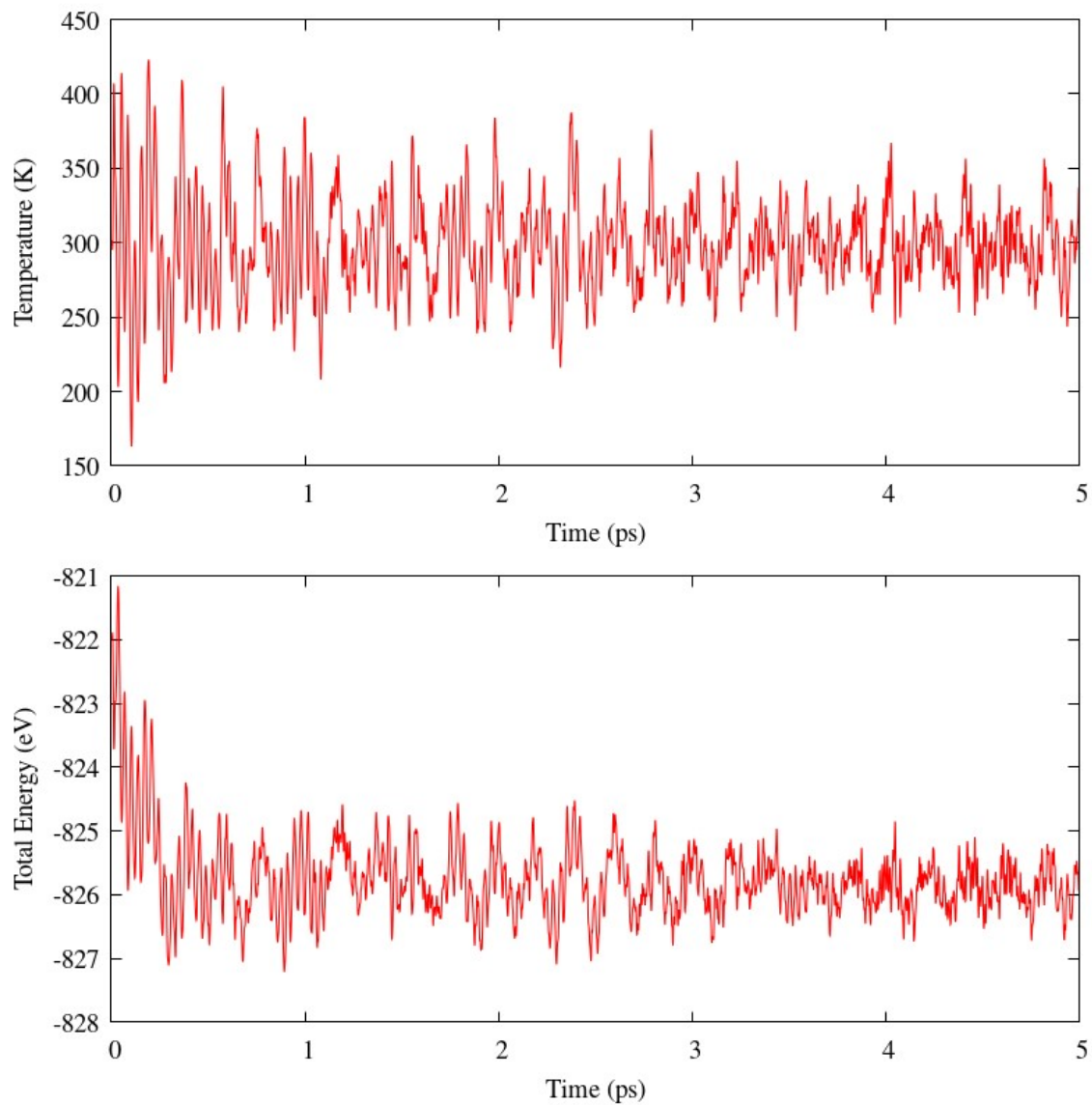


Fig. S18 Temperature vs. time and energy vs full runtime plot for the $Pmn2_1$ structure at 298 K. During this FPMD simulation the structure transitioned to $P2_1/c$.

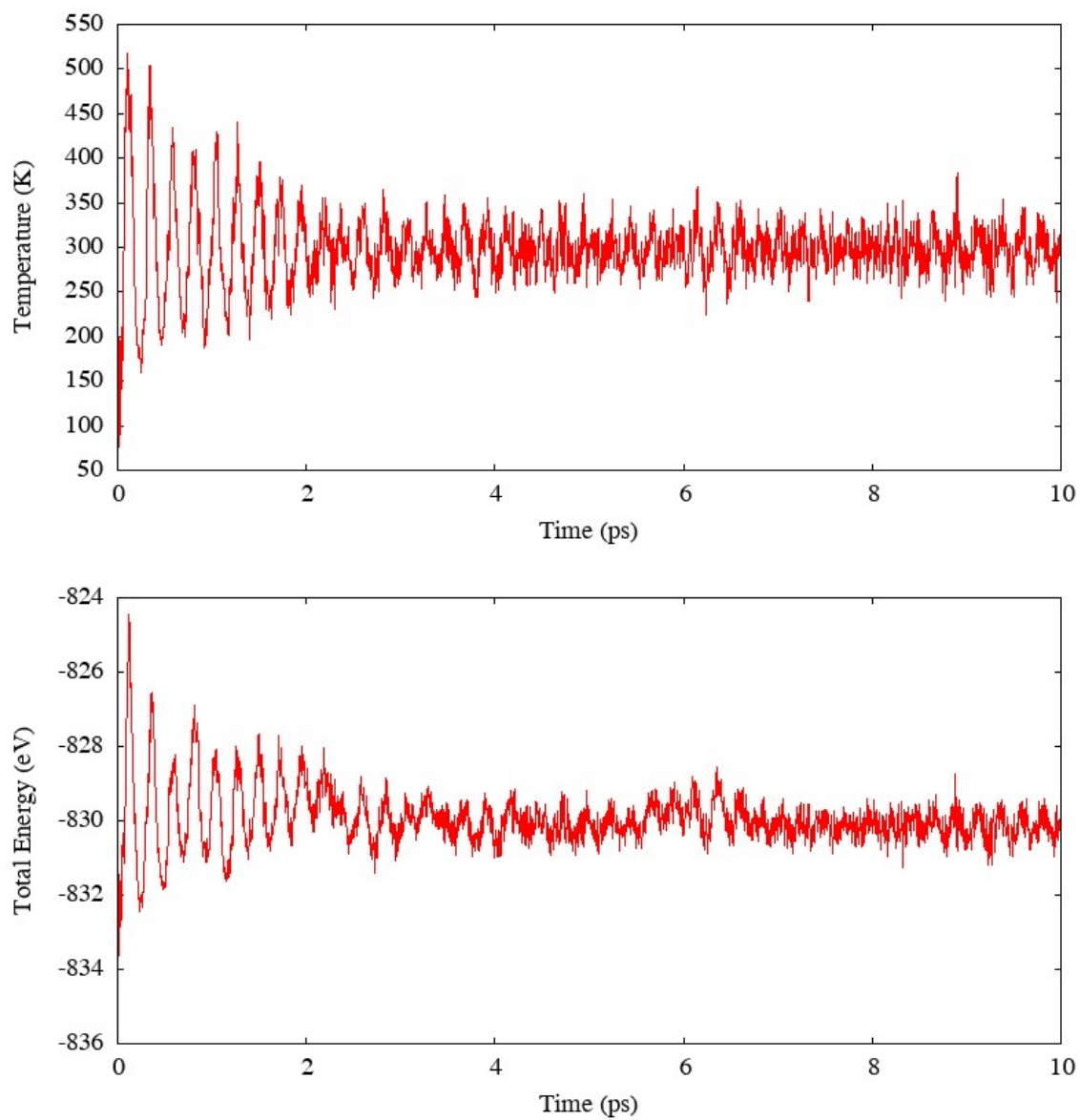


Fig. S19 Temperature vs. time and energy vs full runtime plot for the 2x2x2 supercell $P2_1/c$ system at 298 K.

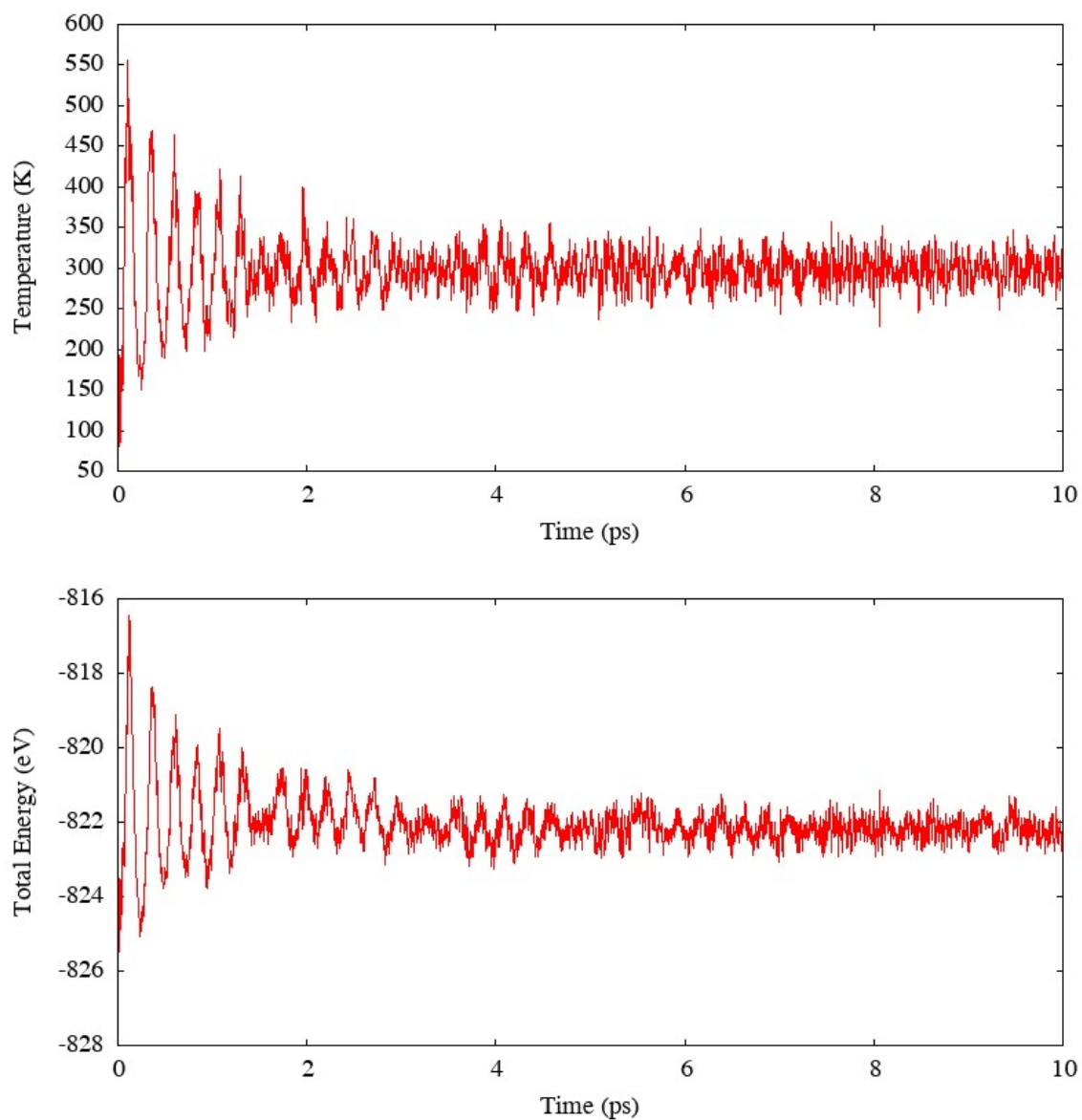


Fig. S20 Temperature vs. time and energy vs full runtime plot for the H1 POCC system at 298 K.

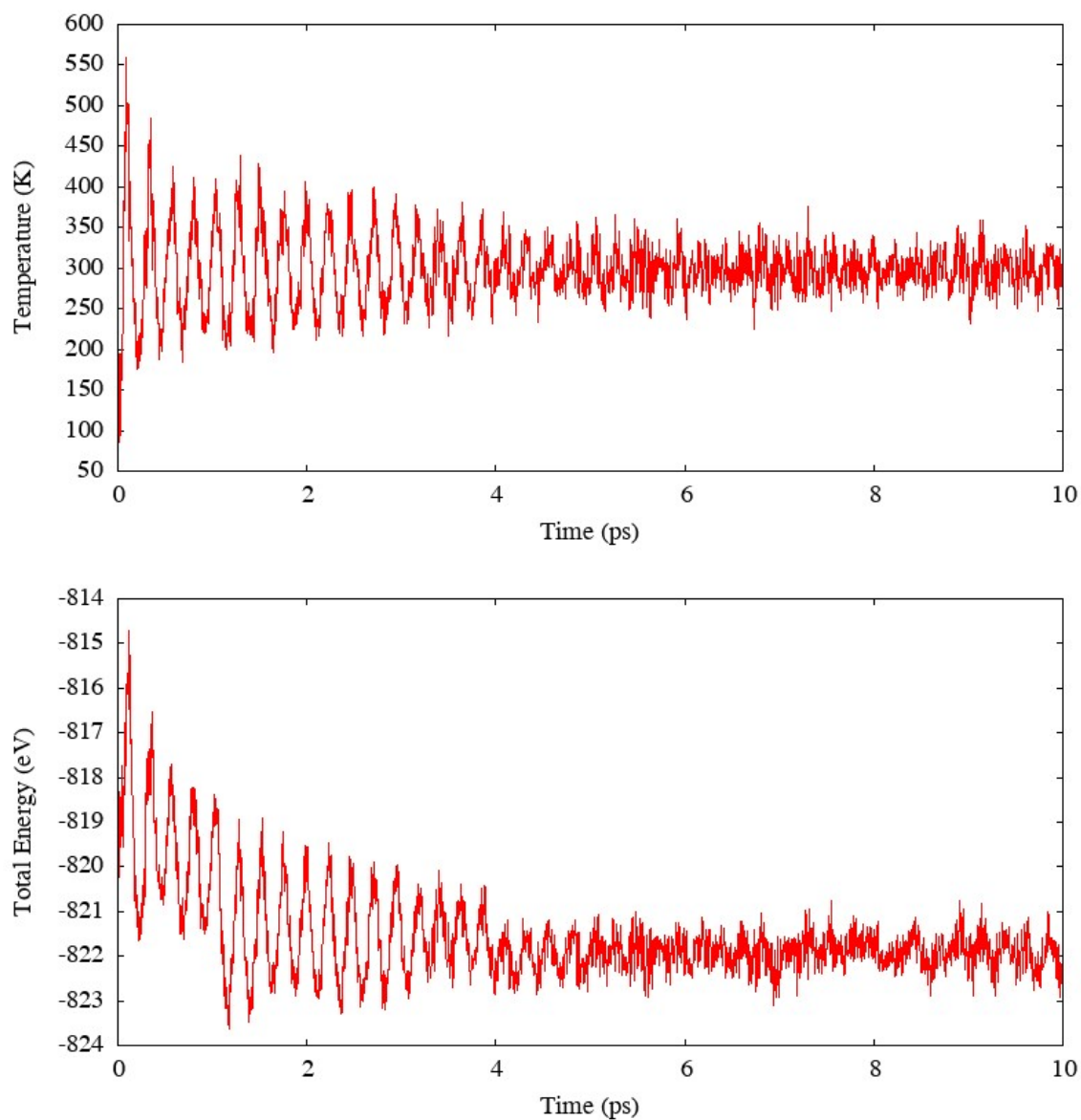


Fig. S21 Temperature vs. time and energy vs full runtime plot for the H2 POCC system at 298 K.

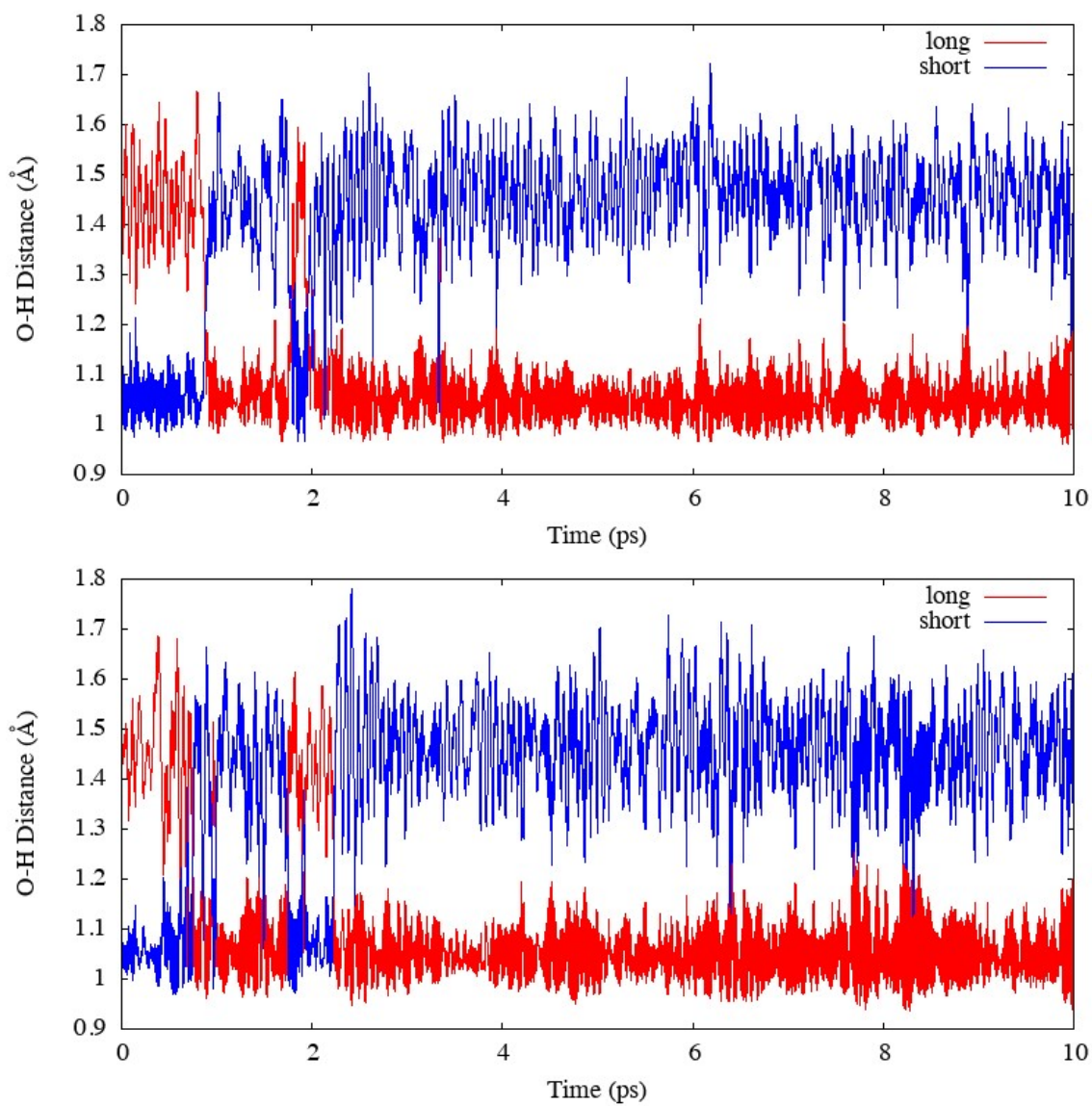


Fig. S22 Two selected O-H bond lengths within the 2x2x2 supercell of the $P2_1/c$ system at 298 K over the full runtime.

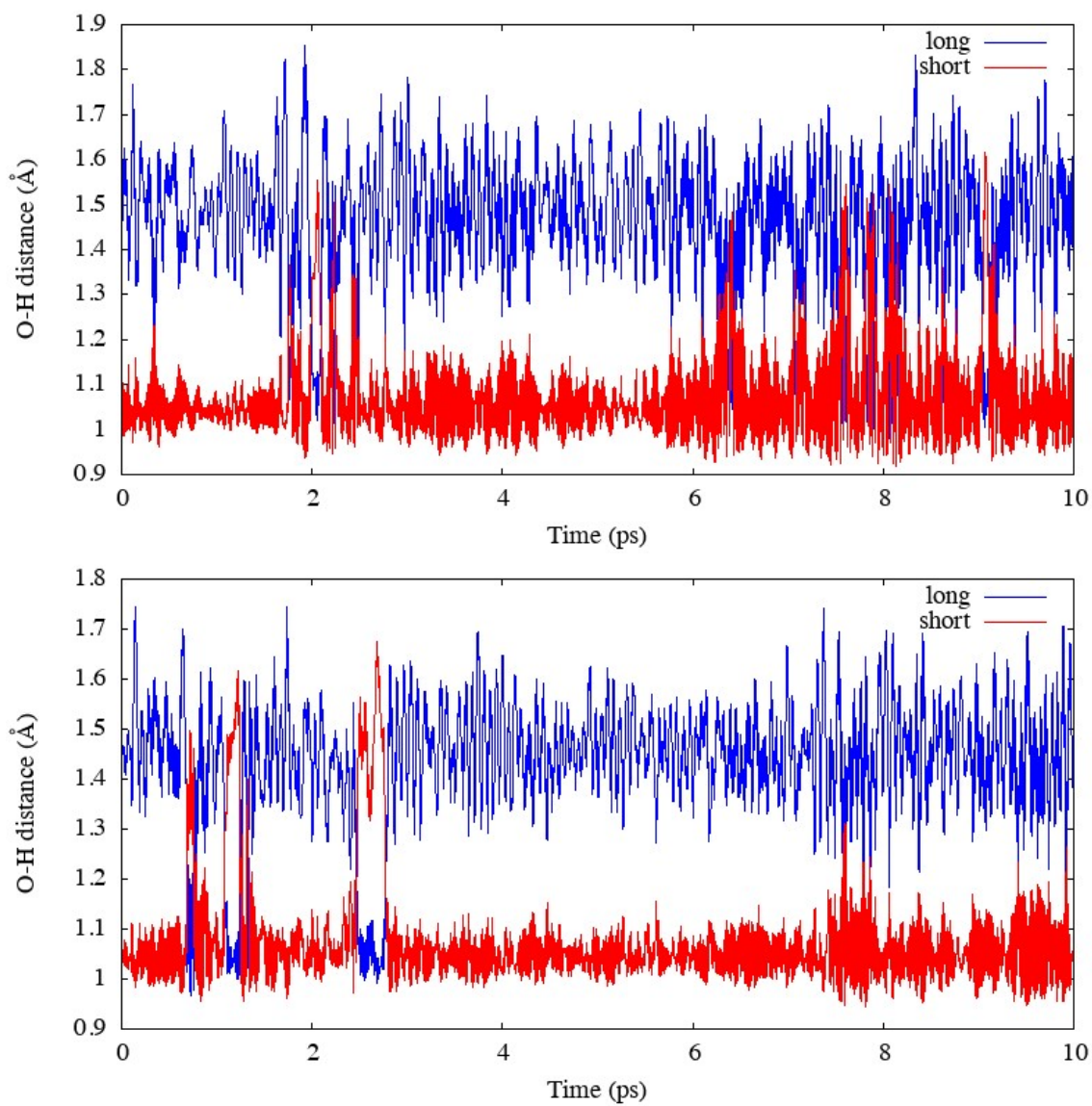


Fig. S23 Two selected O-H bond lengths within the H1 POCC system at 298 K over the full runtime.

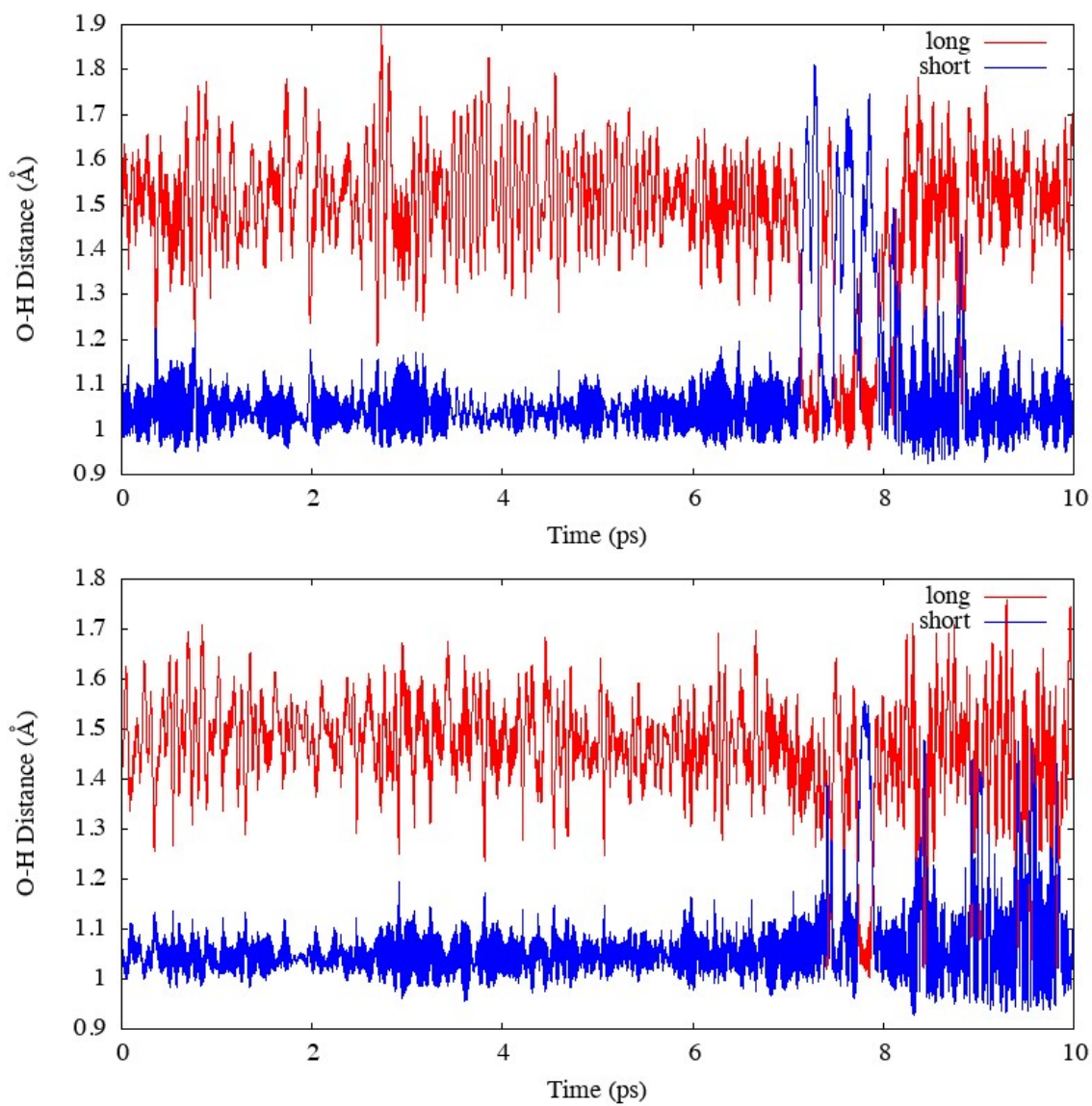


Fig. S24 Two selected O-H bond lengths within the H2 POCC system at 298 K over the full runtime.

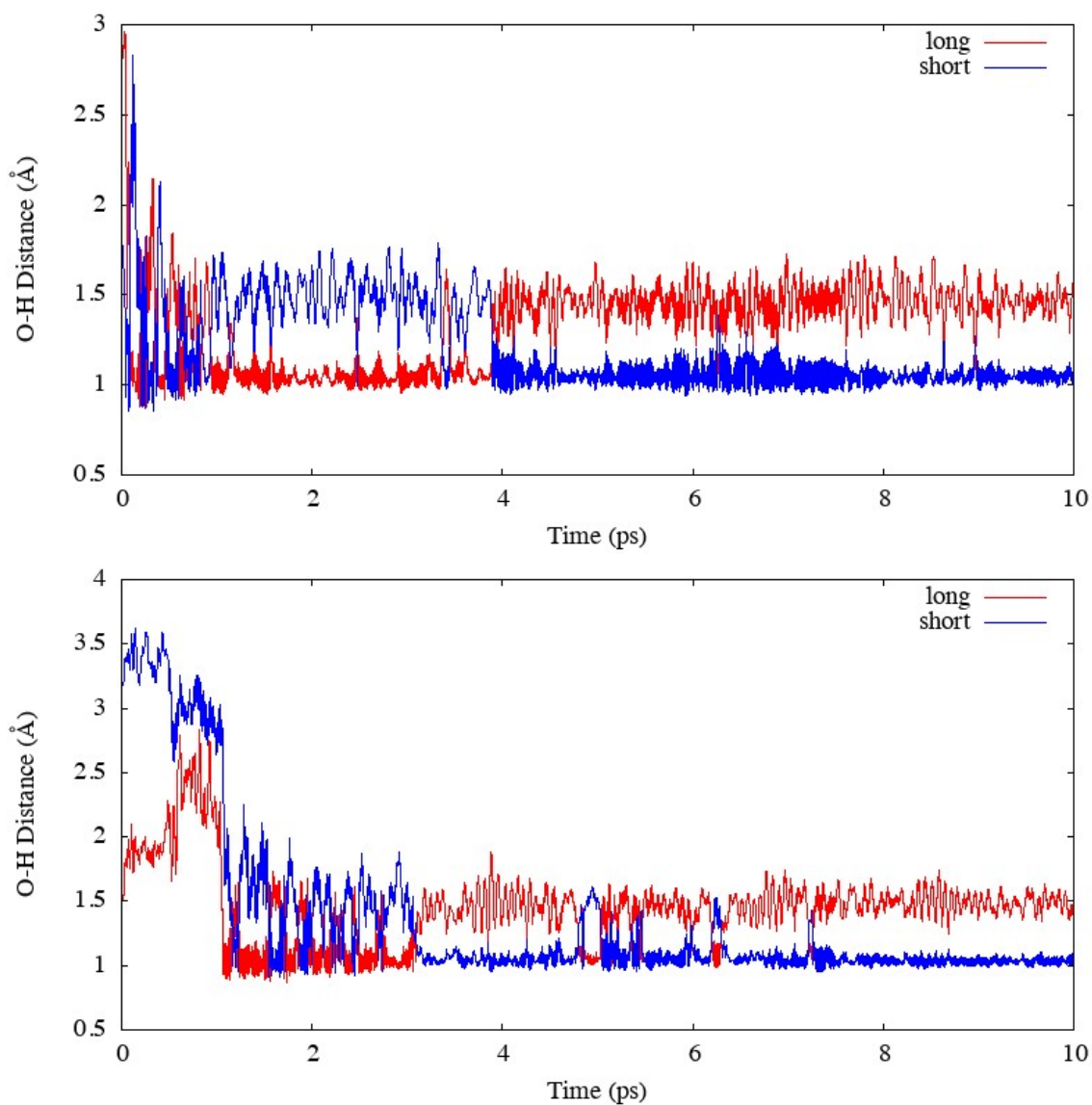


Fig. S25 Two selected O-H bond lengths over the full runtime within the H2 POCC system at 298 K, but for the two protons initially placed so that they comprised Ru-H bonds (the H2 hydrogens). These protons migrated to form hydrogen bonding O-H...O moieties after equilibration.

Table S7. Comparison for the average of all O-H and O...H bond lengths over the full duration of the FPMD runs.

Structure	Temperature (K)	Average O-H Bond Length (Å)	Average O...H Bond Length (Å)
$P2_1/c$	298	1.08	1.38
H1 POCC	298	1.07	1.45
H2 POCC	298	1.10*	1.42*

*Hydrogens not initially bonded to oxygen were not considered in the average.

9. Computational discussion

Structure of $P2_1/c$ RuO₂H, H1 POCC supercell, and H2 POCC supercell

The DFT geometry optimized $P2_1/c$ space group RuO₂H structure, found by relaxing both the unit cell and the atomic positions, has each ruthenium at a coordination number of 6 where 3 of the bonds are with hydroxyl groups, and 3 with oxygen atoms. The experimentally observed unit cell volume of 130.59 Å³ is in excellent agreement with the geometry optimized RuO₂H unit cell volume of 135.95 Å³. Each O-H...O hydrogen bond was computed to lie at an angle of 178° with Ru-O-H-O dihedral angles of 110°. The Ru-O bonds are shorter than the Ru-OH bonds, being 2.03 Å versus 2.14 Å, respectively, with both the oxide and hydroxyl groups having coordination numbers of 3. A phonon calculation performed on the $P2_1/c$ space group RuO₂H displays no imaginary frequencies, as shown in Fig. S17. The projected density of states (PDOS), Fig. S16, possesses primarily Ru ‘d’ and O ‘p’ character in the valence and conduction bands of the semiconductor. The most pronounced H ‘s’ character is observed at ~ -8.5 eV and it mixes with primarily Ru ‘d’ and O ‘p’ associated states.

Structures were constructed as models to study the partial occupancies (POCC) deduced from the XRD refined structure (denoted as H1 and H2). These structures were made by generating a 2x2x2 supercell of the $P2_1/c$ structure (32 formula units total), removing four hydrogens from a particular Ru₄O₈H₄ unit within it and adding two hydrogen atoms either at the H1 or at the H2 positions. These POCC models have a stoichiometry of RuO₂H_{0.9375}. During the structural optimization of the H1 structure, the hydrogens moved from the midpoint between the two oxygen atoms yielding roughly an O-H...O configuration. Upon optimization of the H2 POCC structure such a rearrangement does not occur. The computed range of O...H distances of 1.6 Å – 1.9 Å fits with the experimental range observed, and the three centered hydrogen bonding character in the experimental H2 position is preserved during relaxation. The simulated XRD patterns of the RuO₂H, POCC H1, and POCC H2 models display close resemblance to the experimental XRD spectra.

Nudged elastic band modeling

In order to assess the dynamics and mobility of the hydrogens in RuO_2H , nudged elastic band (NEB) calculations were performed to locate maxima along the O-H...O to O...H-O transfer paths. All attempts at transferring a single hydrogen atom were unsuccessful and are assumed to be disallowed, as a single H transition leaves one Ru coordinated to four hydroxyls and two oxides and another Ru coordinated to two hydroxyls and four oxides. When all of the hydrogens (4H) were transferred simultaneously in the RuO_2H unit cell, the barrier was calculated to be 37 meV/atom as shown in Fig. S10. The maximum energy geometry for the 4H NEB had each hydrogen 1.21 Å from its two interacting oxygens, at the midpoint between the oxygens. Further computational exploration of the hydrogenic transition unveiled a stepwise 2H – 2H transfer mechanism, that pushes two hydrogens across from O-H...O into O...H-O moieties, followed by an additional transfer of two hydrogens. This results in two barriers, each being 19 meV/atom, as shown in Fig. S11. In the maximum energy structure along the reaction profile in the 2H – 2H transfer mechanism, the hydrogen atoms are also located at the midpoint between the oxygens, having an O-H distance of 1.21 Å as in the 4H model. Having a concerted transfer mechanism results in a barrier that is approximately half as high, just by reducing the number of hydrogen atoms moving simultaneously. Lastly, a 1x2x1 supercell was constructed from the RuO_2H conventional cell and a 2H – 2H – 2H – 2H transfer mechanism was explored with NEB calculations. Remarkably, the barrier was found to be even smaller at 10 meV/atom, with intermediates that lay 6 meV/atom higher in energy than the ground state, illustrated in Fig. S12. The hydrogen atoms in the intermediates were found to lie slightly off center from the midpoint, with O-H distances measuring 1.23 Å and 1.19 Å. The intermediates are similar to the starting $P2_1/c$ RuO_2H crystal but with four of the eight O-H bonds lengthening to 1.06 Å. Such a lowering of the barrier upon enlarging the model cell implies that the barrier would continue to lower upon consecutive NEB calculations with larger supercells. Indeed, as shown by our first principles molecular dynamics (FPMD) calculations, at room temperature hydrogen transfers occur spontaneously.

First principles molecular dynamics of $P2_1/c$ RuO_2H , H1 POCC, and H2 POCC supercells

First principles molecular dynamics (FPMD) simulations were performed on 2x2x2 supercell models of the $P2_1/c$ RuO_2H , H1 POCC, and H2 POCC structures at 298 K in NVT ensembles for 10 ps. Plots of selected O-H bond distance versus time over the course of the FPMD runs for all three structures are provided in Fig. S22-S25. For each FPMD simulation, a proton transfer duration was obtained by determining how long a proton was closer to the oxygen it was not initially bonded to, indicative of proton transfer. This was found by using the O-H and O...H bond lengths relative to the midpoint between the two oxygen atoms. See Table S7 for a quantitative representation of the time spent during proton transfer in the FPMD runs in a percentage format. The $P2_1/c$ RuO_2H structure displays O-H distances that lengthen to approximately 1.4 - 1.6 Å at

particular time intervals. The H...O distances shorten to approximately 1.1 Å. This lengthening and shortening of O-H and H...O bonding is indicative of proton transfer. Some protons repeatedly engage in transfer, while others maintain their short O-H bond lengths. The H1 POCC and H2 POCC O-H bond lengths undergo the same effect observed in RuO₂H, albeit with the H2 POCC having a longer transfer duration. The FPMD data supports the conclusion from the NEB data in that proton transfers are readily accessible in the RuO₂H system whether partially or fully occupied.

Notably, near the beginning of the H2 POCC FPMD run the proton at the H2 site that is initially bonded to Ru (Ru-H bond length of 1.66 Å) quickly migrates to form an O-H...O bond, suggesting that such a phase is thermally unstable. It may be that molecular hydrogen (H₂) binds to Ru in a side-on fashion, and via H₂ σ → Ru d and Ru d → H₂ σ* donation and back-donation, thereby breaking the H-H bond. The protons then migrate to form bonds with oxygen. Further calculations that are beyond the scope of this project would be required to probe this hypothesis.

Table S8: The percentage of post-equilibration time over the course of the FPMD run associated with a structure where a proton transferred from its original O-H...O to an O...H-O position. The percentages were obtained by dividing the proton transfer duration by the post-equilibration time and multiplying by 100%. *Hydrogens not initially bonded to oxygen were not considered in the percentage.

FPMD % Proton Transfer Duration	<i>P</i> _{21/c} RuO ₂ H	H1 POCC	H2 POCC
Time Percentage (%)	2.50%	2.52%	6.44%*

Raman, NMR, and Bader charges

DFPT calculated Raman spectra of *P*_{21/c} RuO₂H reveal an O-H vibration at 2273 cm⁻¹, which is not in agreement with the absence of a peak at this frequency associated with an O-H vibration in experiment. Unsurprisingly, calculations on the maximum structure found using the NEB method where all protons were undergoing proton transfer (4H), Fig. S14, did not possess a signal past ~1500 cm⁻¹ as no O-H bond was present. Our calculations using classical nuclei suggest that proton transfer in this double well potential should be relatively facile. Anharmonic and quantum nuclear effects, which are past the scope of the work presented here, are likely to further enhance the probability of proton transfer. In a realistic system the proton transfer will decrease the intensity and broaden the peak associated with the O-H stretch in the Raman spectrum. Moreover, it is known that when the frequency associated with the O-H...O stretch falls below 2700 cm⁻¹, its intensity decreases nearly zero in experiment.²¹

NMR chemical shifts of the protons relative to tetramethylsilane were calculated for the

relaxed $P2_1/c$ RuO_2H structure, as well as the relaxed H1 POCC and H2 POCC phases with $\text{RuO}_2\text{H}_{0.9375}$ stoichiometries. The average shifts of the protons involved in O-H...O bonds were calculated to be 13.5 ppm, 14.5 ppm and 15.5 ppm, respectively. In the H2 POCC structure there is an additional proton that is bonded to Ru (Ru-H distance of 1.63 Å). Its chemical shift was calculated to be 1.1 ppm. A similar calculation was performed using a structure snapshot taken after 1 ps of the $P2_1/c$ FPMD simulation. These values increased to 14.4 ppm, 15.6 ppm and 16.7 ppm, respectively, with the Ru-H becoming an O-H...O bond and deshielding significantly within the H2 POCC phase. The computed ^1H NMR chemical shift of these protons relative to tetramethylsilane (TMS) is in good agreement with experimental and DFT data for molecules with similar asymmetry parameters for protons in resonance-assisted hydrogen bonds²², and somewhat lower than the value of 14.7 ppm observed here. Calculations on the maximum structure found using the NEB method where all protons were undergoing proton transfer (4H, Fig. S10) with the proton placed in the midpoint between two oxygen atoms ($D_{\text{OHO}} = 0$) yielded a shift of 20.7 ppm, similar to values obtained for the hydrogen succinate anion whose $D_{\text{OHO}} = 0.13$ ²².

V. Supplementary references

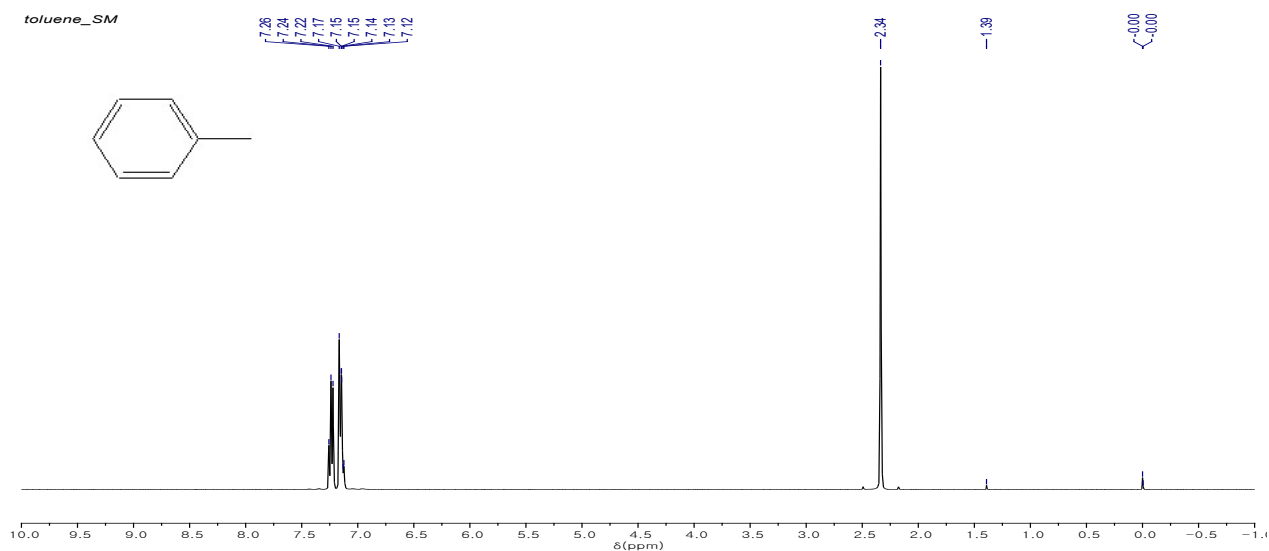
1. F. B. Su, L. Lv, F. Y. Lee, T. Liu, A. I. Cooper and X. S. Zhao, *J. Am. Chem. Soc.* 2007, **129**, 14213–14223.
2. F. B. Su, L. Lv, F. Y. Lee, T. Liu, A. I. Cooper and X. S. Zhao, *Acta Phys. -Chim. Sin.* 2016, **32**, 1765–1774.
3. W. Qian, L. N. Lin, Y. X. Qiao, X. G. Zhao, Z. C. Xu, H. H. Gong, D. F. Li, M. Y. Chen, R. Huang and Z. S. Hou, *Appl. Catal., A* 2019, **585**, 117183.
4. M. Takasaki, Y. Motoyama, K. Higashi, S. H. Yoon, I. Mochida and H. Nagashima, *Chem. Asian J.* 2007, **2**, 1524–1533.
5. K. X. Yao, X. Liu, Z. Li, C. C. Li, H. C. Zeng and Y. Han, *ChemCatchem* 2012, **4**, 1938–1942.
6. Q. Pei, T. He, Y. Yu, Z. J. Jing, J. P. Guo, L. Liu, Z. T. Xiong and P. Chen, *ACS Appl. Mater. Interfaces* 2020, **12**, 7071–7080.
7. D. C. Lonie and E. Zurek, *Comput. Phys. Commun.* 2011, **182**, 372–387.
8. Z. Falls, P. Avery, X. Y. Wang, K. P. Hilleke and E. Zurek, *J. Phys. Chem. C* 2021, **125**, 1601–1620.
9. P. Avery, Z. Falls and E. Zurek, *Comput. Phys. Commun.* 2018, **222**, 418–419.
10. G. Henkelman, B. P. Uberuaga and H. Jonsson, *J. Chem. Phys.* 2000, **113**, 9901–9904.
11. G. Kresse and J. Furthmuller, *Phys. Rev. B* 1996, **54**, 11169–11186.
12. G. Kresse and D. Joubert, *Phys. Rev. B* 1999, **59**, 1758–1775.
13. J. P. Perdew, K. Burke and M. Ernzerhof, *Phys. Rev. Lett.* 1996, **77**, 3865–3868.
14. P. E. Blöchl, *Phys. Rev. B* 1994, **50**, 17953–17979.

15. H. J. Monkhorst and J. D. Pack, *Phys. Rev. B* 1976, **13**, 5188–5192.
16. A. Togo, F. Oba and I. Tanaka, *Phys. Rev. B* 2008, **78**, 134106.
17. D. Porezag and M. R. Pederson, *Phys. Rev. B* 1996, **54**, 7830–7836.
18. A. Fonari and S. Stauffer, <https://github.com/raman-sc/VASP/> 2013
19. S. Y. Mar, C. S. Chen, Y. S. Huang and K. K. Tiong, *Appl. Surf. Sci.* 1995, **90**, 497–504.
20. Y. S. Huang and F. H. Pollak, *Solid State Commun.* 1982, **43**, 921–924.
21. B. A. Kolesov, *Int. J. Mol. Sci.* 2021, **22**, 5380.
22. K. Sutter, G. A. Aucar and J. Autschbach, *Chem. Eur. J.* 2015, **21**, 18138–18155.

VI. Supplementary data

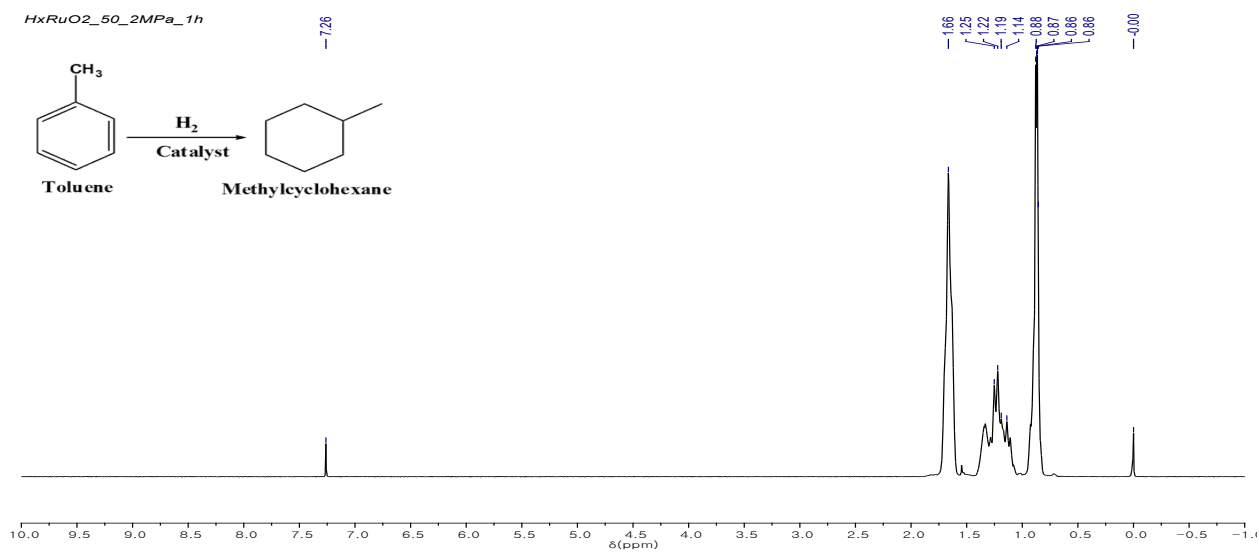
^1H NMR spectral copies and characterization data for all the compounds. (Table 1, Table 2, Table 3, Table S4)

[Starting reagent – Toluene]



Toluene ^1H NMR (400 MHz, CDCl_3) δ 7.25 (m, 1H), δ 7.17 (m, 1H), δ 2.36 (s, 3H)

[Table 1, entry 1]



Methylcyclohexane ^1H NMR (400 MHz, CDCl_3) δ 1.71-1.58 (m, 5H), δ 1.33 (m, 1H), δ 1.22 (m, 2H), δ 1.12 (m, 1H), δ 0.87 (m, 2H), δ 0.86 (d, 3H)

[Table 1, entry 2]

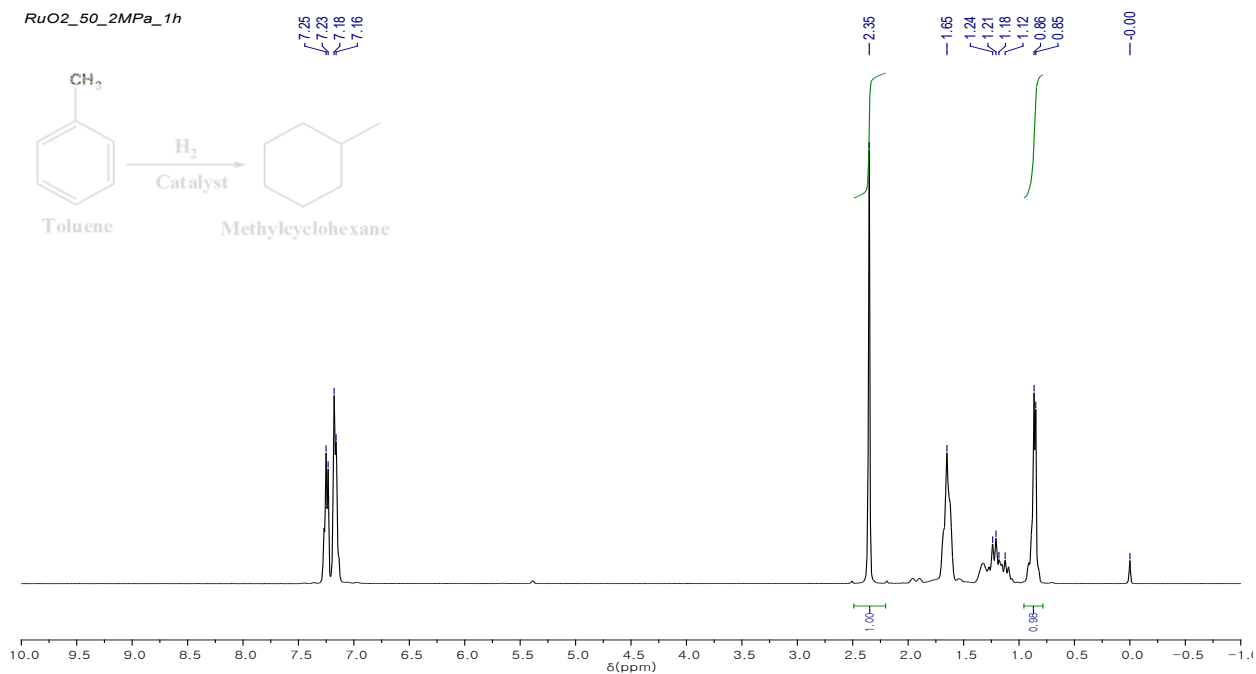


[Table 1, entry 3]

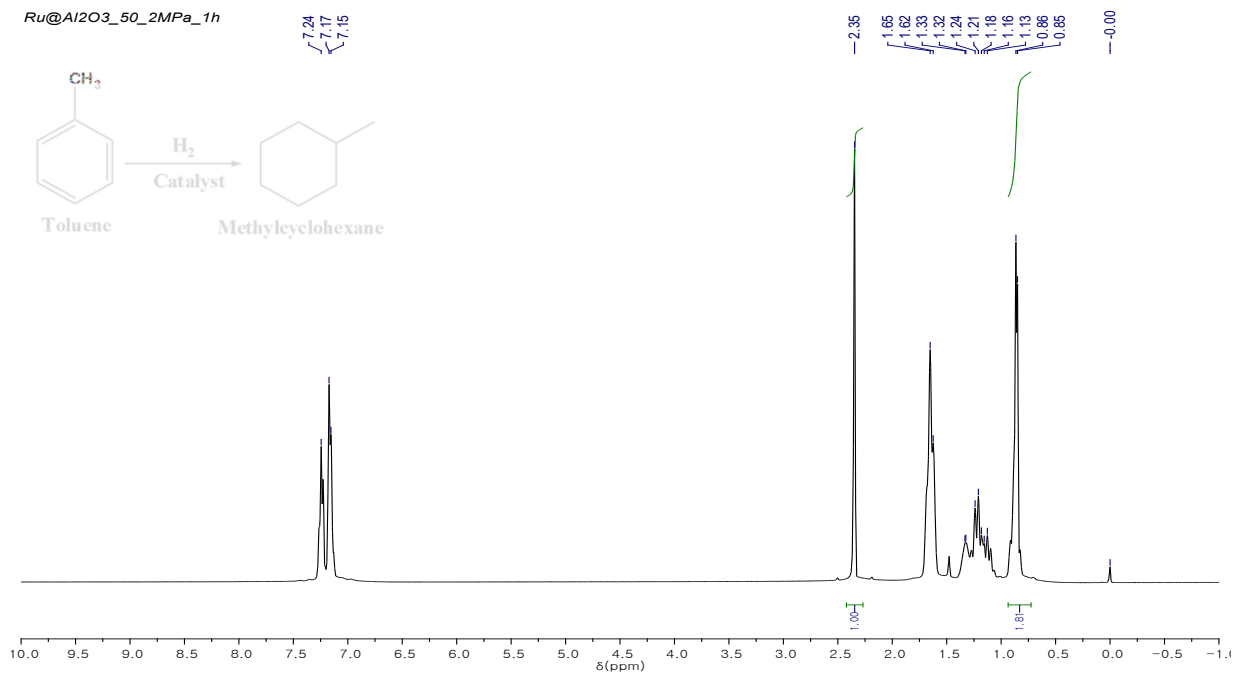


[Table 1, entry 4]

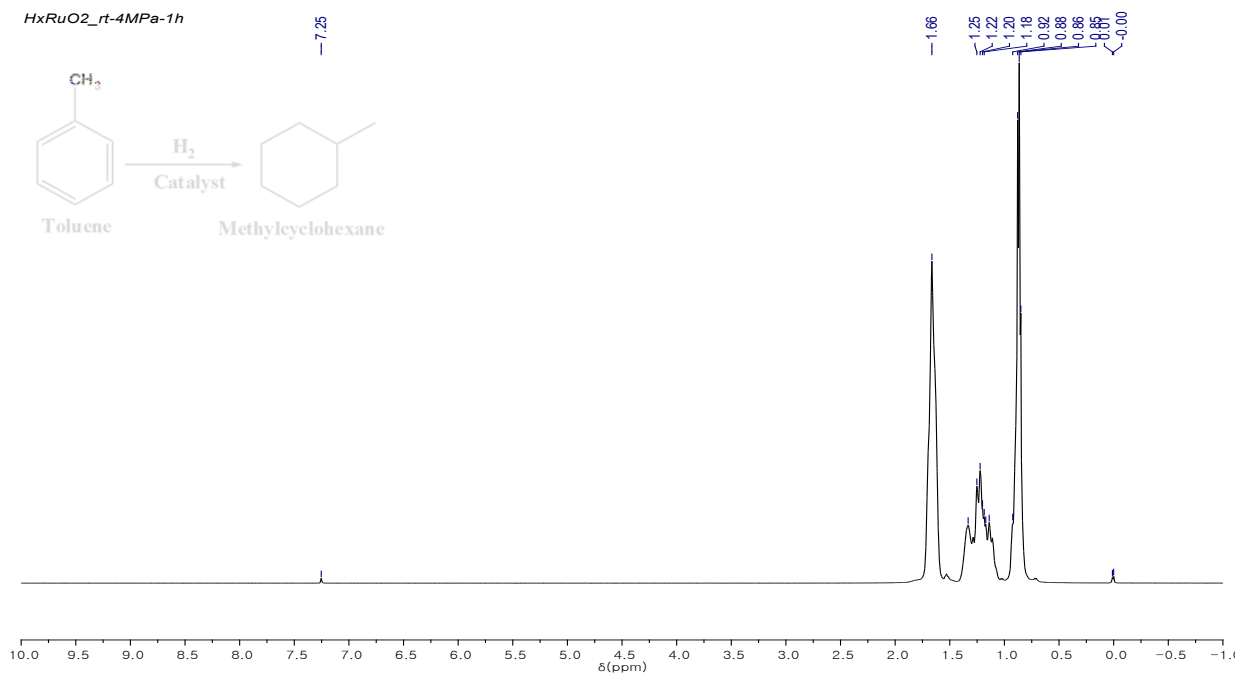


[Table 1, entry 5]

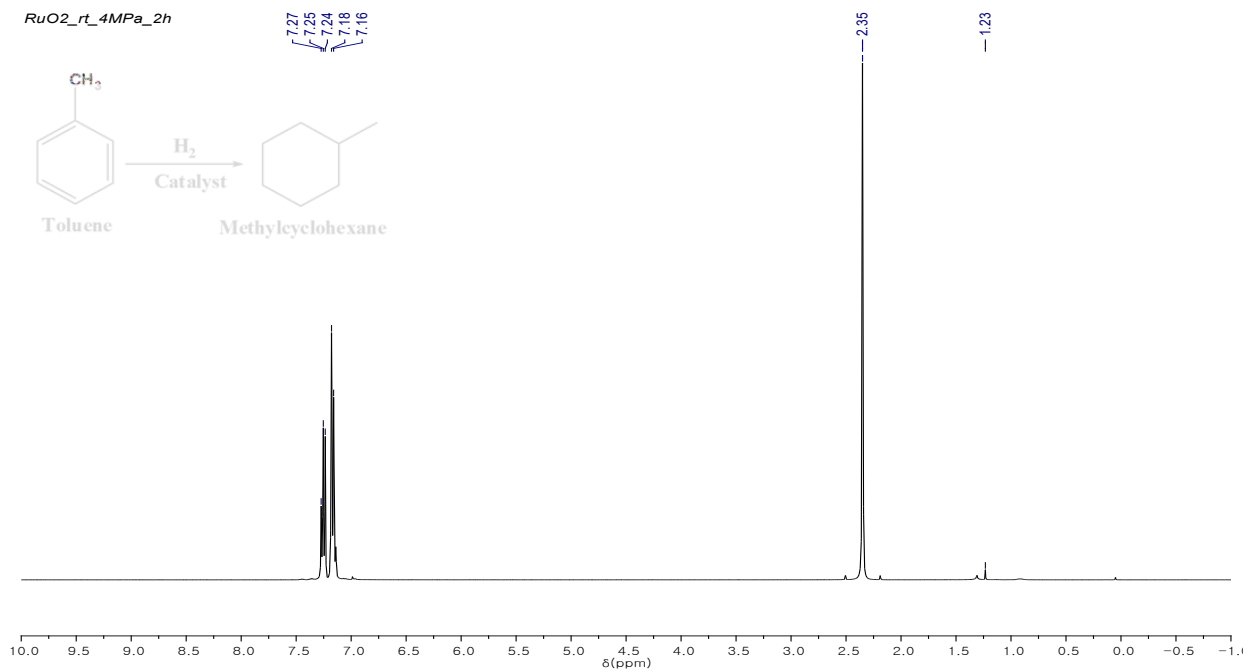


[Table 1, entry 6]

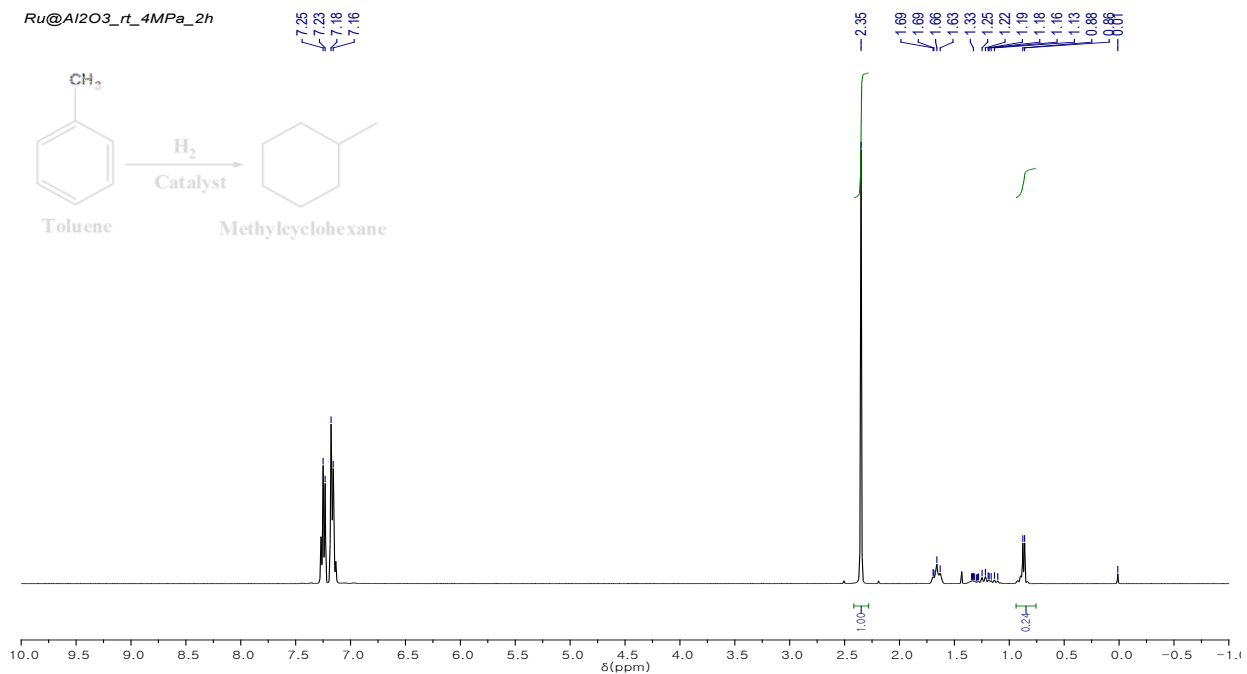
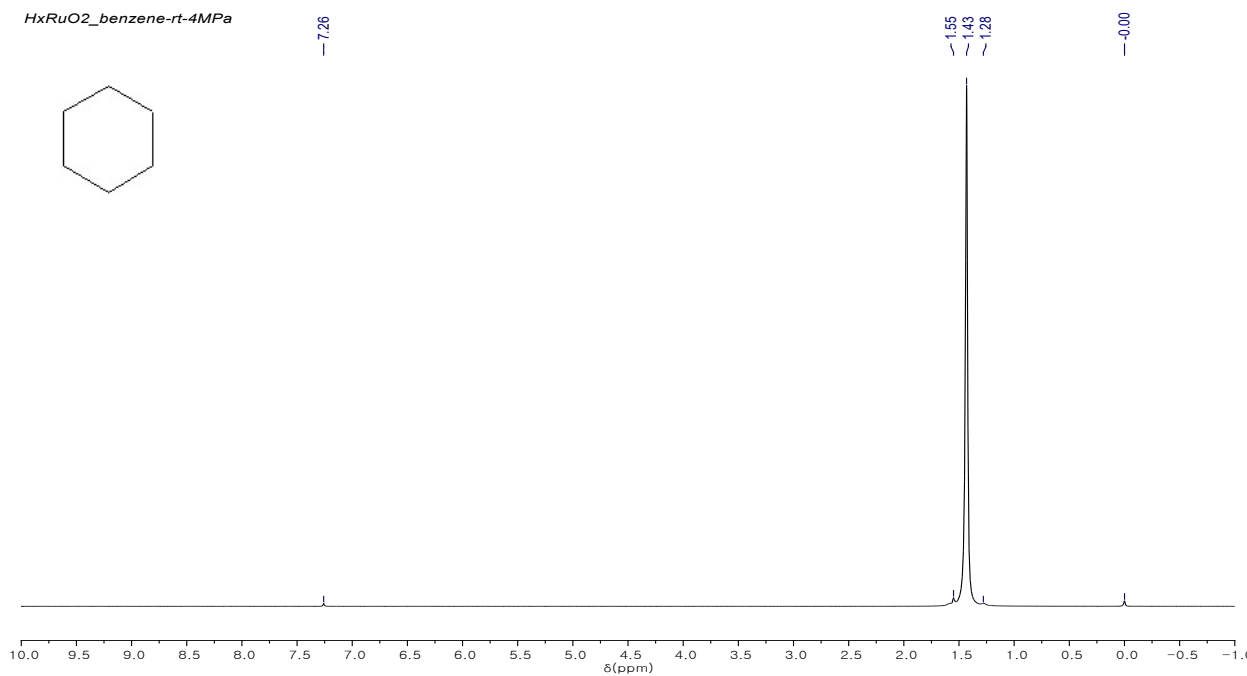
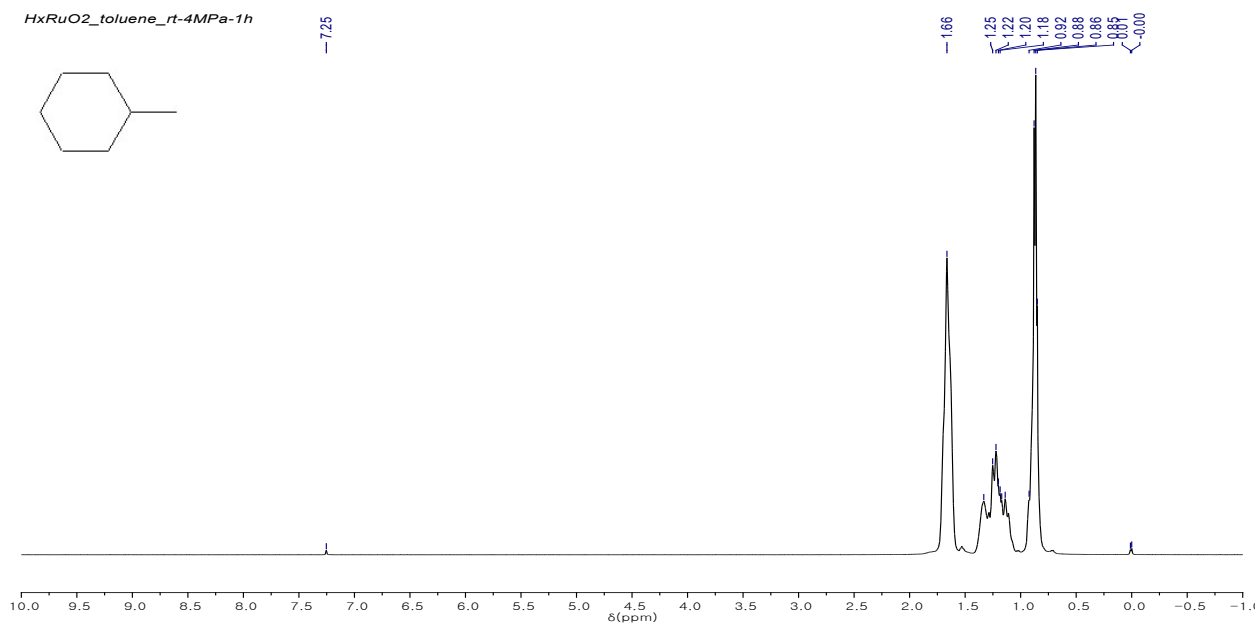


[Table 2, entry 1]



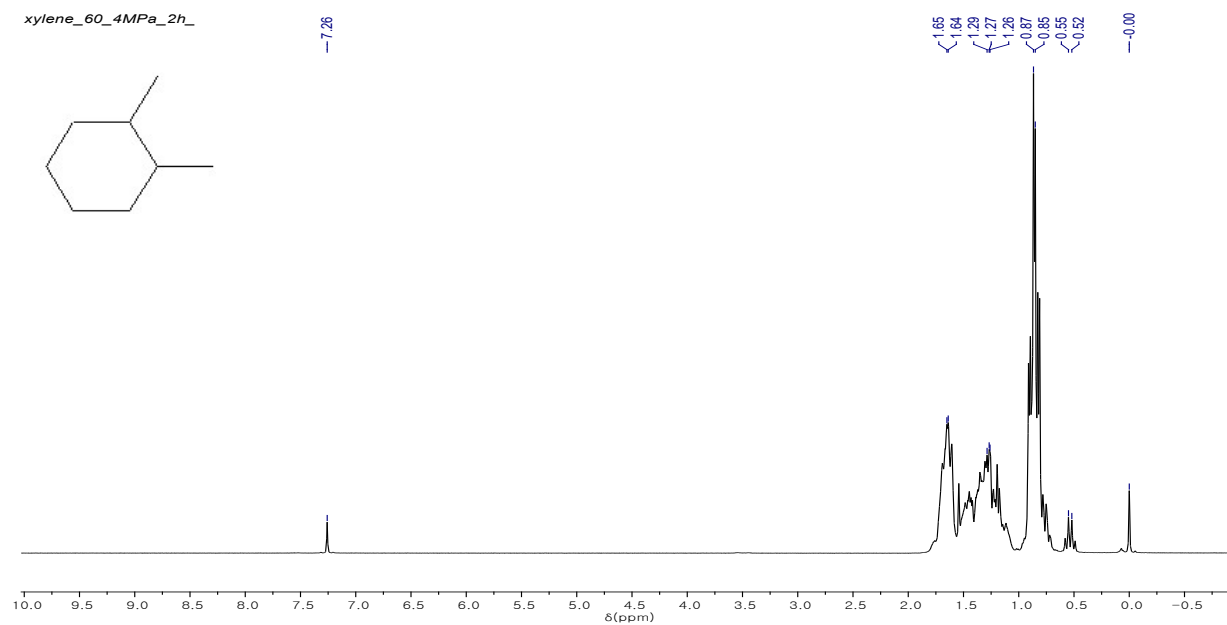
Cyclohexane ^1H NMR (400 MHz, CDCl_3) δ 1.43 (s, 12H)

[Table 2, entry 2]



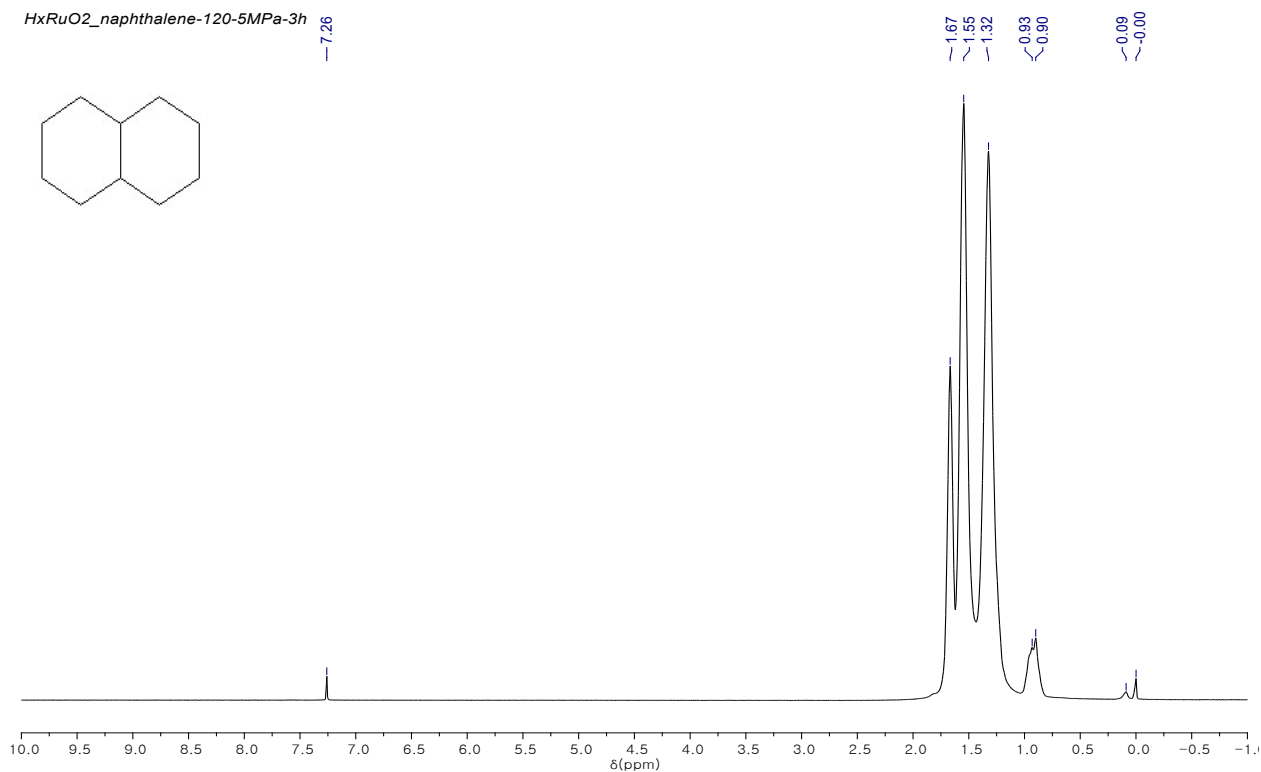
Methylcyclohexane ^1H NMR (400 MHz, CDCl_3) δ 1.71-1.58 (m, 5H), δ 1.33 (m, 1H), δ 1.22 (m, 2H), δ 1.12 (m, 1H), δ 0.87 (m, 2H), δ 0.86 (d, 3H)

[Table 2, entry 3]



1,2-Dimethylcyclohexane ^1H NMR (400 MHz, CDCl_3) δ 1.60 (m, 2H), δ 1.28-1.53 (m, 8H), δ 0.96 (m, 6H)

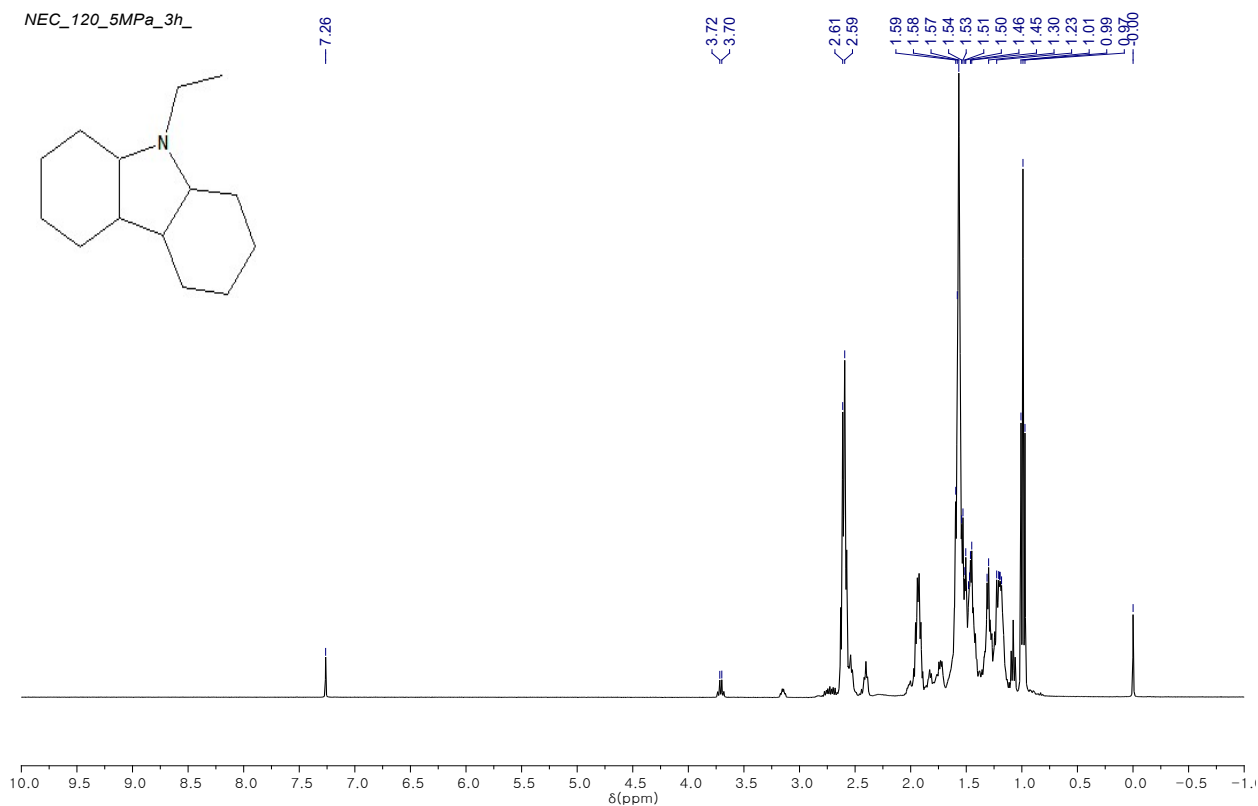
[Table 2, entry 4]



***cis*-Decalin** ¹H NMR (400 MHz, CDCl₃) δ 1.70 (m, 2H), δ 1.64 (m, 2H), δ 1.59 (m, 2H), δ 1.45 (m, 4H), δ 1.38 (m, 2H), δ 1.32 (m, 2H), δ 1.19 (m, 2H), δ 1.18 (m, 2H)

***trans*-Decalin** ¹H NMR (400 MHz, CDCl₃) δ 1.67 (m, 4H), δ 1.54 (m, 4H), δ 1.25 (m, 4H), δ 0.93 (m, 4H), δ 0.88 (m, 4H)

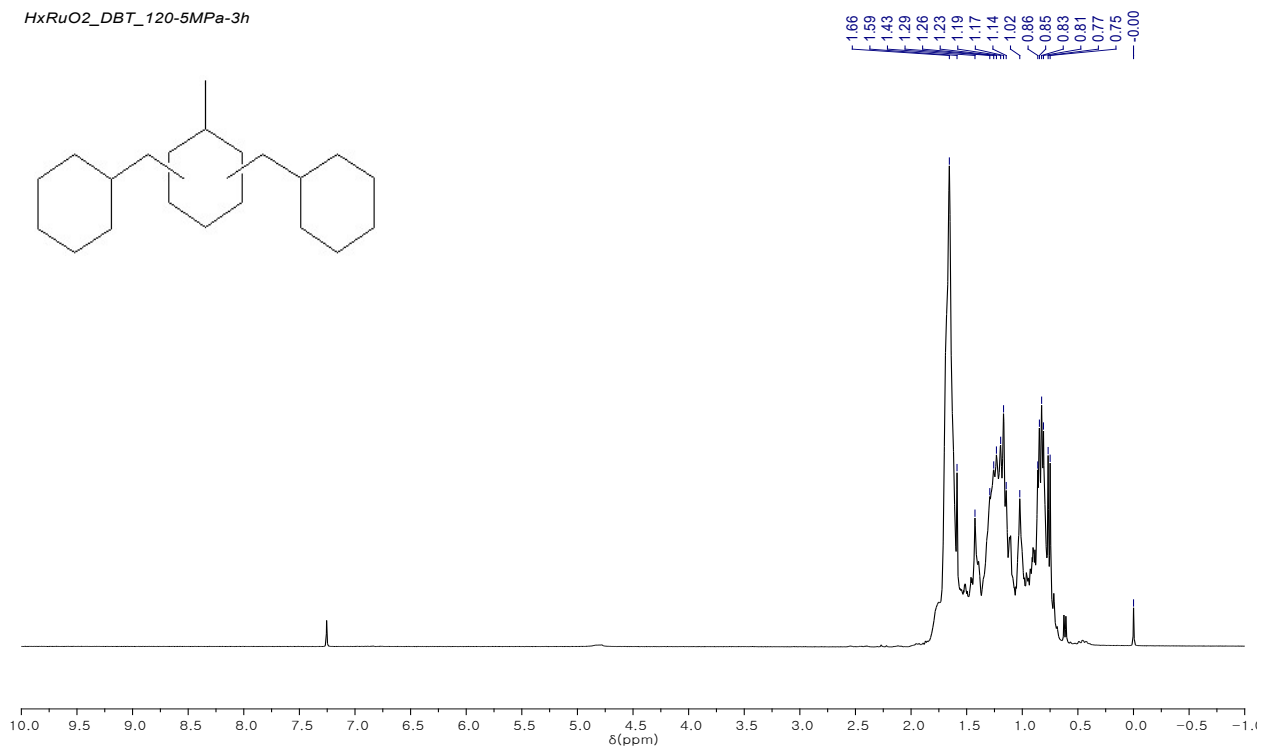
[Table 2, entry 5]



9-Ethyldecahydro-1H-carbazole (12H-NEC) ^1H NMR (400 MHz, CDCl_3) δ 2.40 (q, 2H), δ 2.06 (m, 2H), δ 1.65 (m, 2H), δ 1.58 (m, 2H), δ 1.53 (m, 4H), δ 1.43 (m, 2H), δ 1.33 (m, 2H), δ 1.28 (m, 2H), δ 1.21 (m, 2H), δ 1.11 (m, 2H), δ 1.02 (t, 3H)

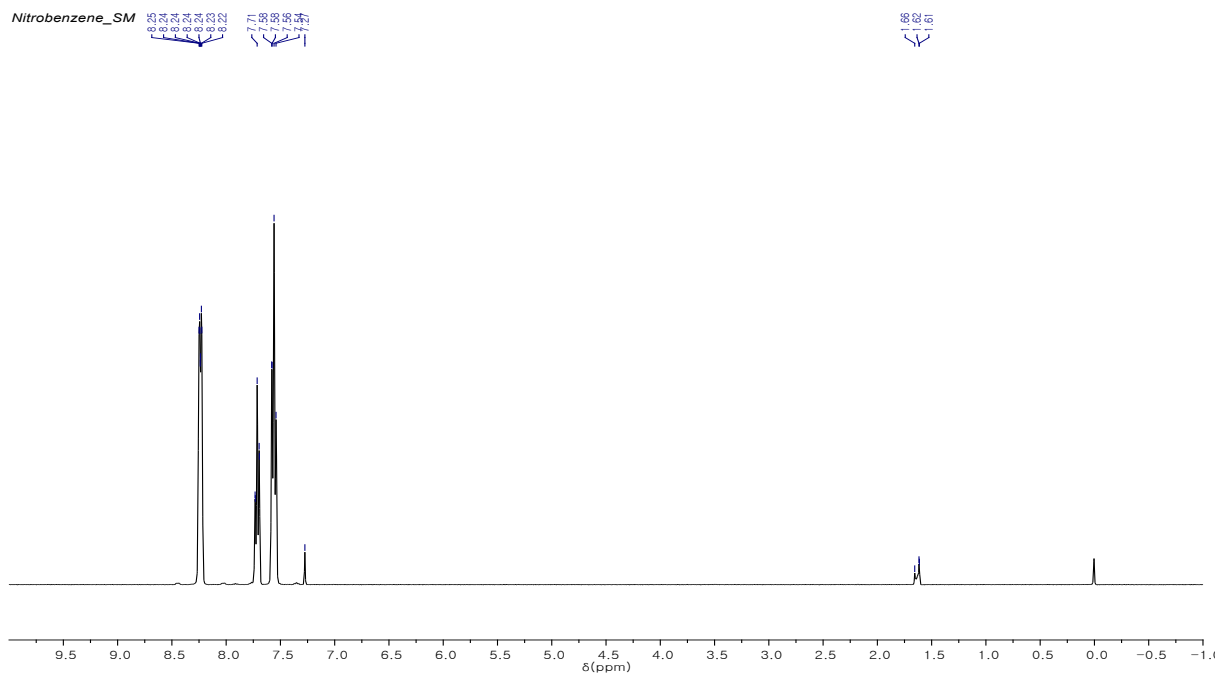
[Table 2, entry 6]

HxRuO2_DBT_120-5MPa-3h



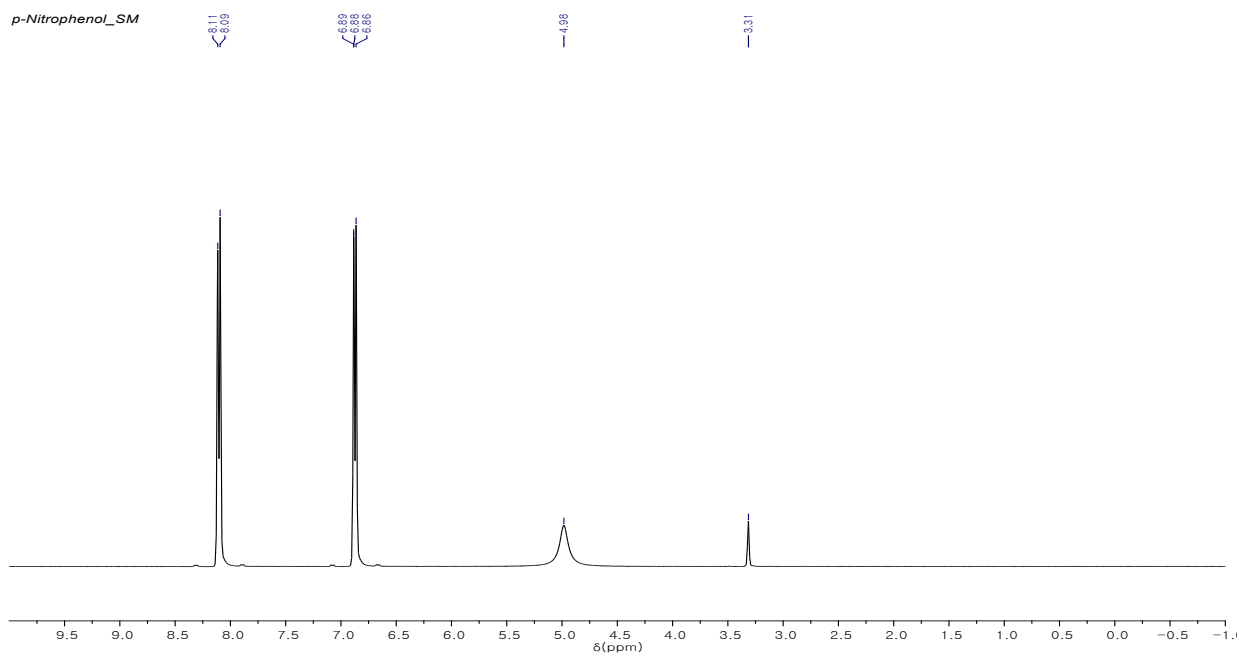
18H-Dibenzyltoluene ^1H NMR (400 MHz, CDCl_3) δ 1.59 (m, 1H), δ 1.53 (m, 11H), δ 1.49 (m, 2H), δ 1.47 (m, 2H), δ 1.43 (m, 7H), δ 1.42 (m, 2H), δ 1.28 (m, 6H), δ 1.21 (m, 4H), δ 0.96 (d, 3H)

[Starting reagent – Nitrobenzene]



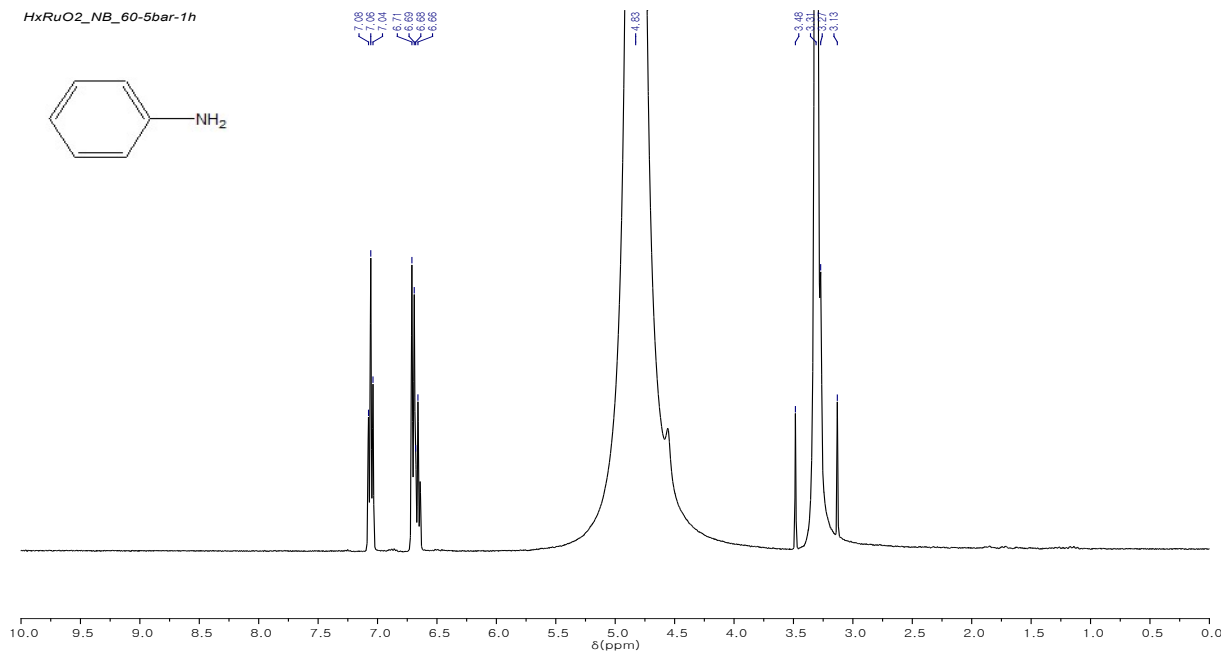
Nitrobenzene ^1H NMR (400 MHz, CDCl_3) δ 8.26 (d, 2H), δ 7.71 (q, 2H), δ 7.45 (q, 1H)

[Starting reagent – p-Nitrophenol]



p-Nitrophenol ^1H NMR (400 MHz, CD_3OD) δ 8.10 (d, 2H), δ 6.88 (d, 2H)

[Table 3, entry 1]



Aniline ¹H NMR (400 MHz, CD₃OD) δ 7.06 (q, 2H), δ 6.70 (q, 1H), δ 6.65 (d, 2H)

[Table 3, entry 2]

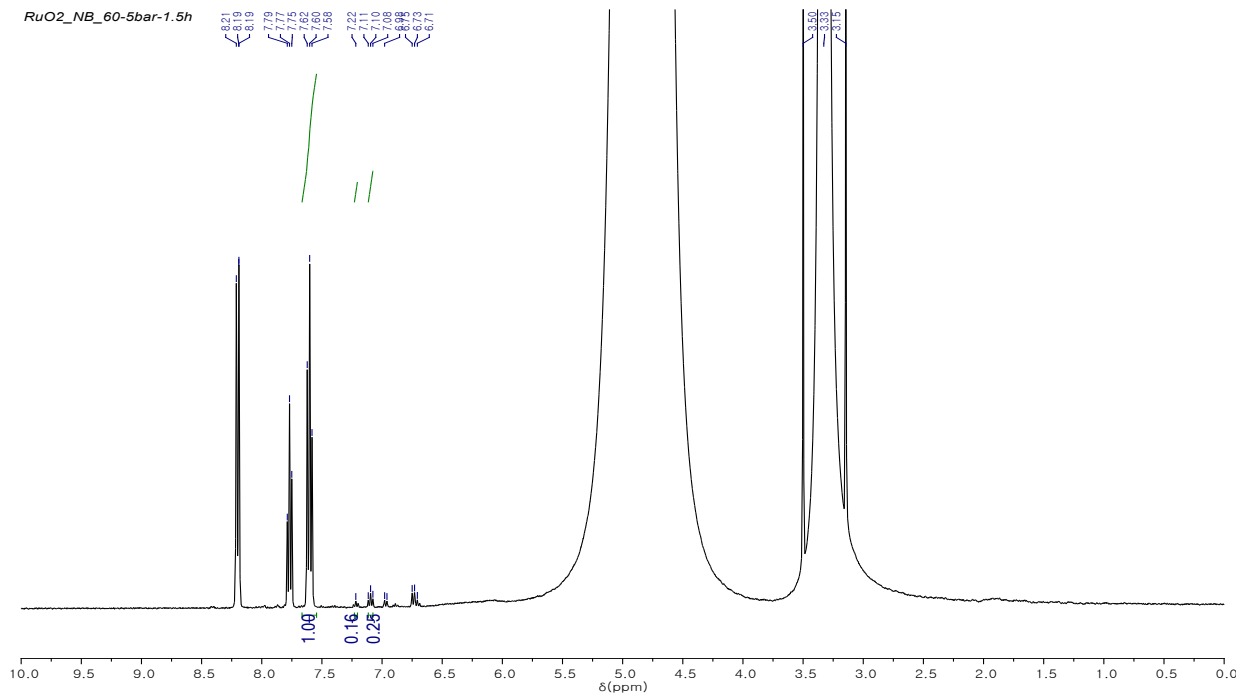


[Table 3, entry 3]

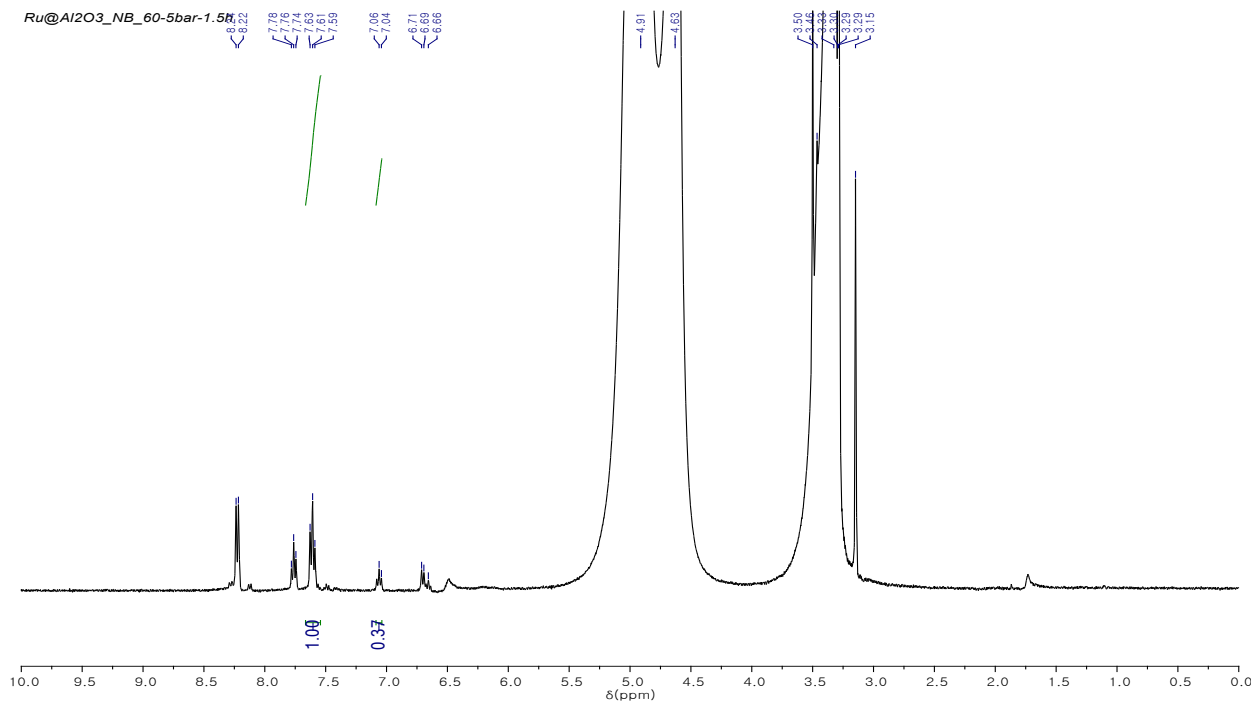
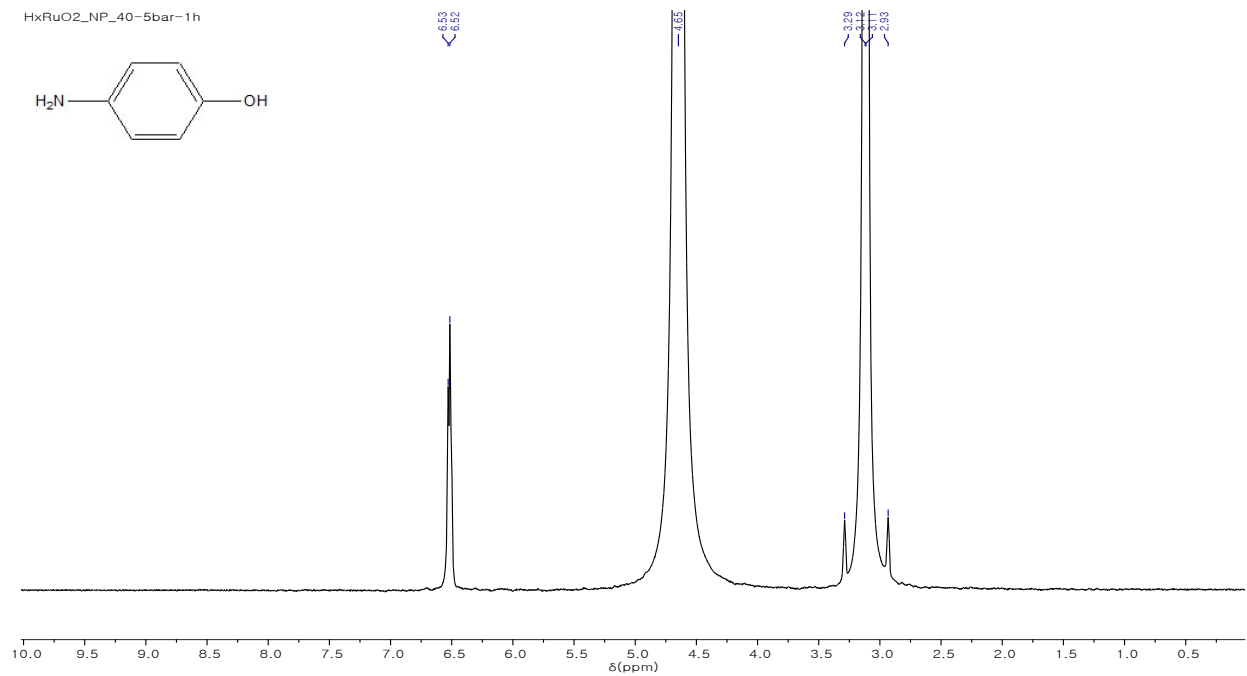


[Table 3, entry 4]



p-Aminophenol ¹H NMR (400 MHz, CD₃OD) δ 6.60 (d, 2H), δ 6.50 (d, 2H)

[Table 3, entry 5]

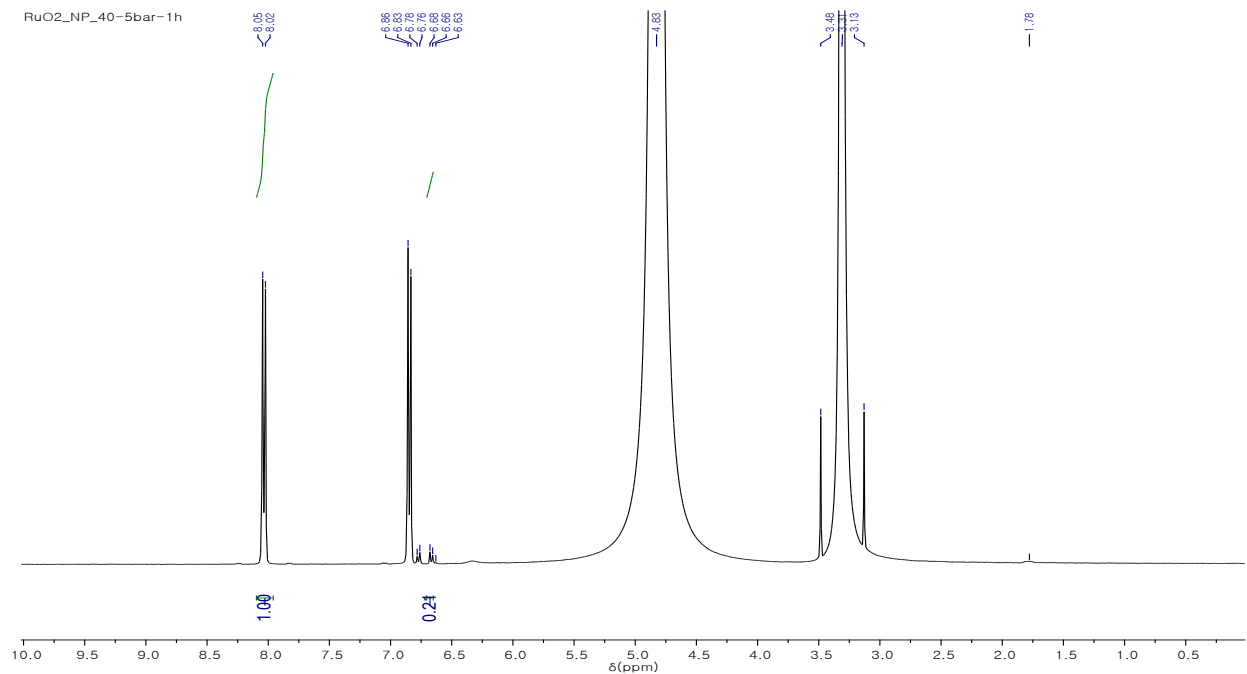


[Table 3, entry 6]

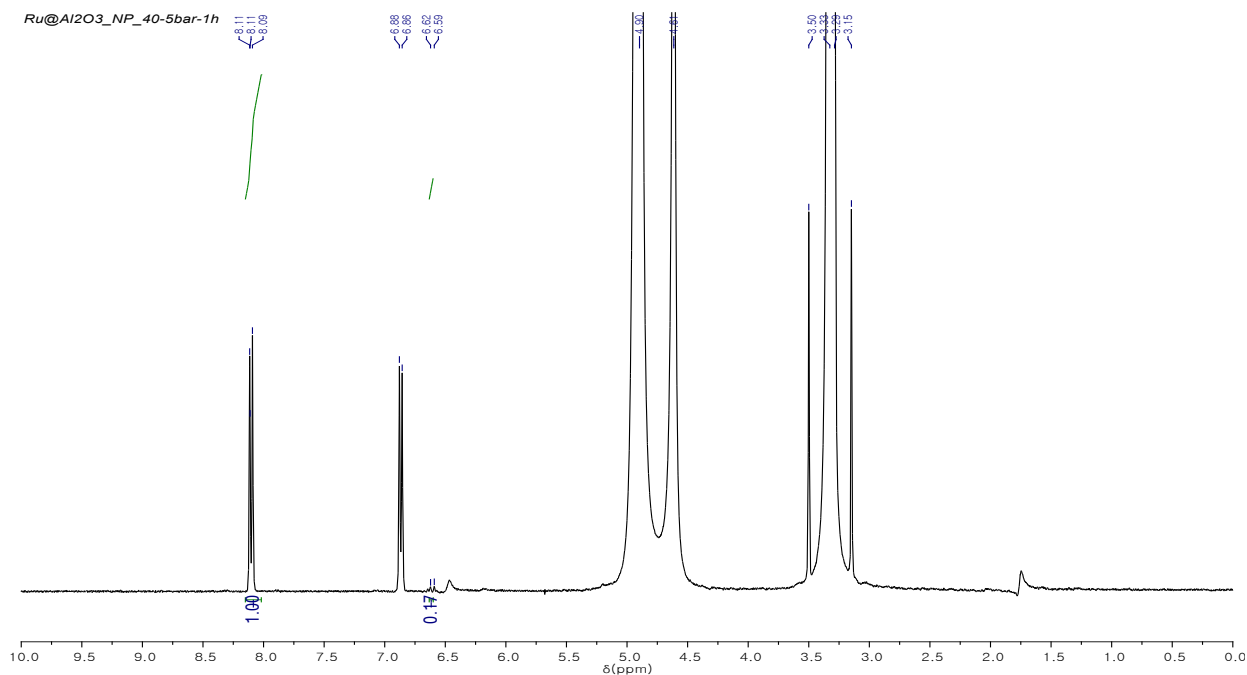
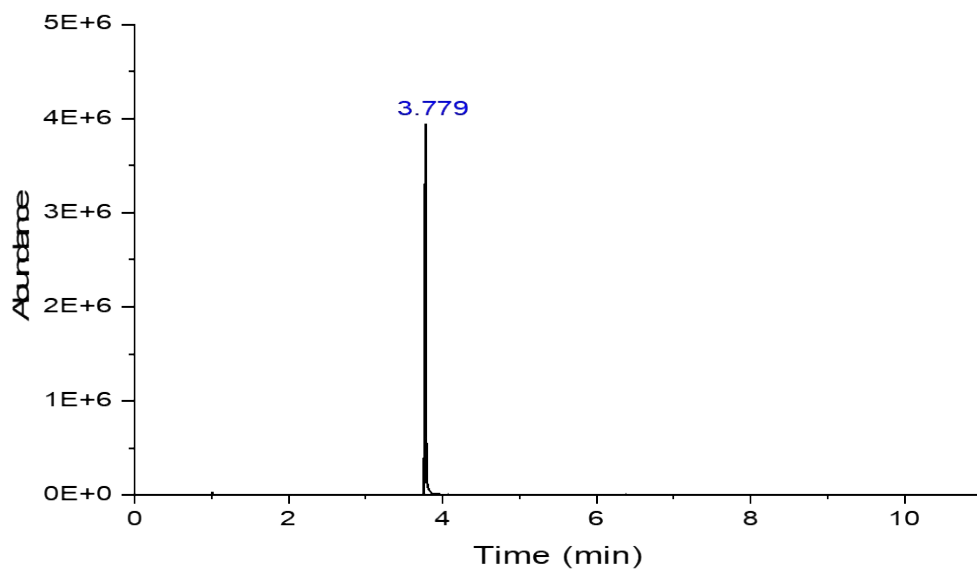
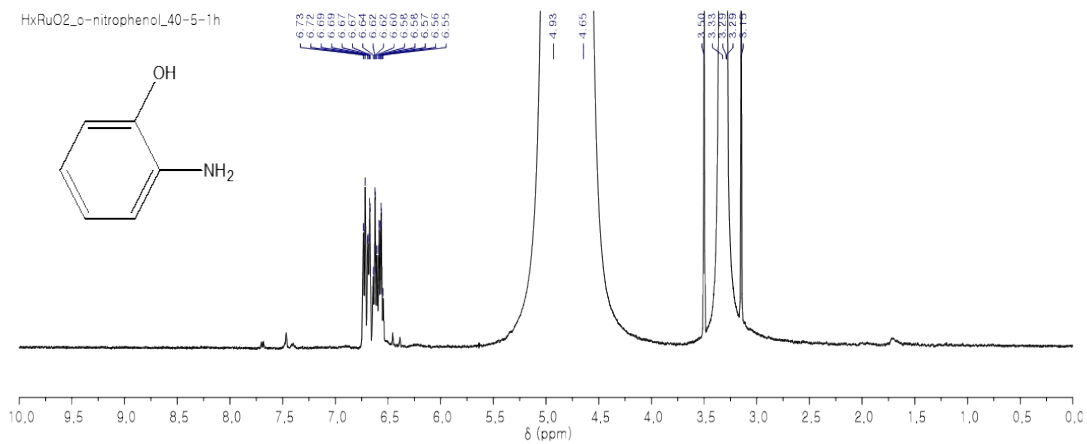


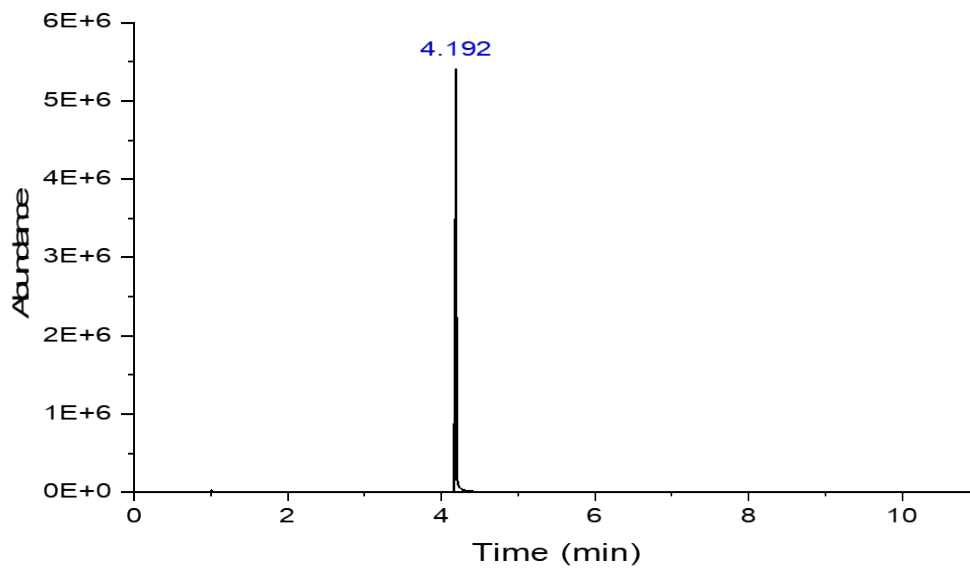
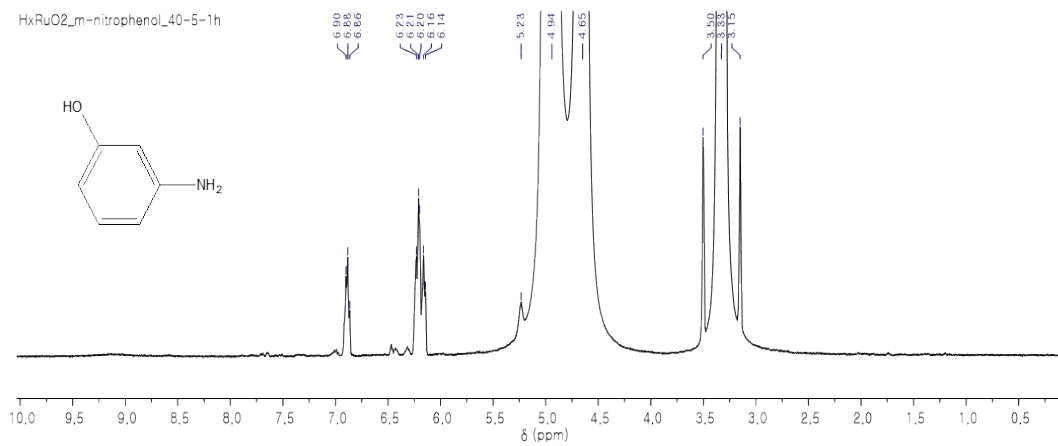
[Table S4, entry 1]



o-Aminophenol ^1H NMR (400 MHz, CD_3OD) δ 6.72 (q, 1H), δ 6.68 (q, 1H), δ 6.62 (d, 1H), δ 6.55 (d, 1H)

Retention time: 3.779 min (o-aminophenol)

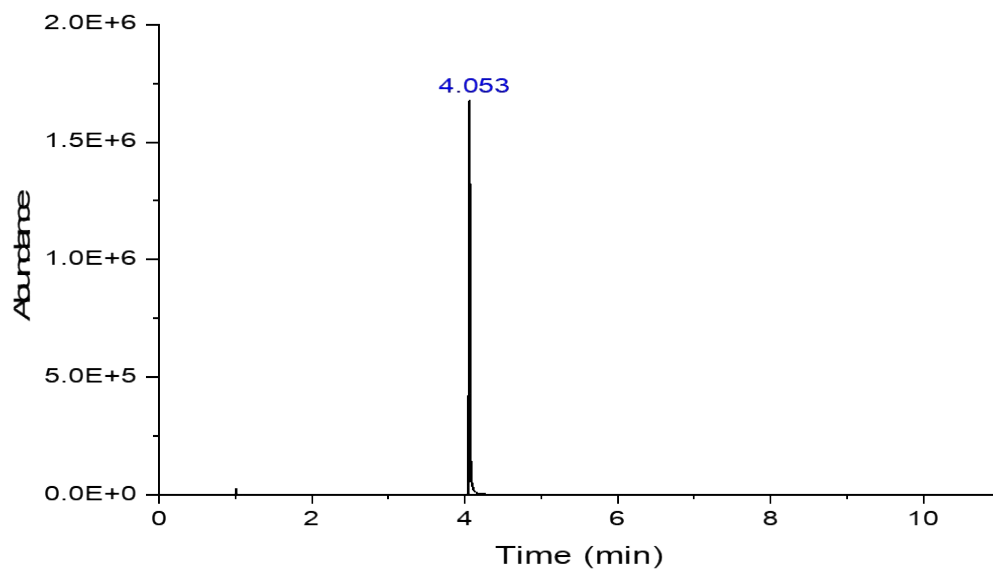
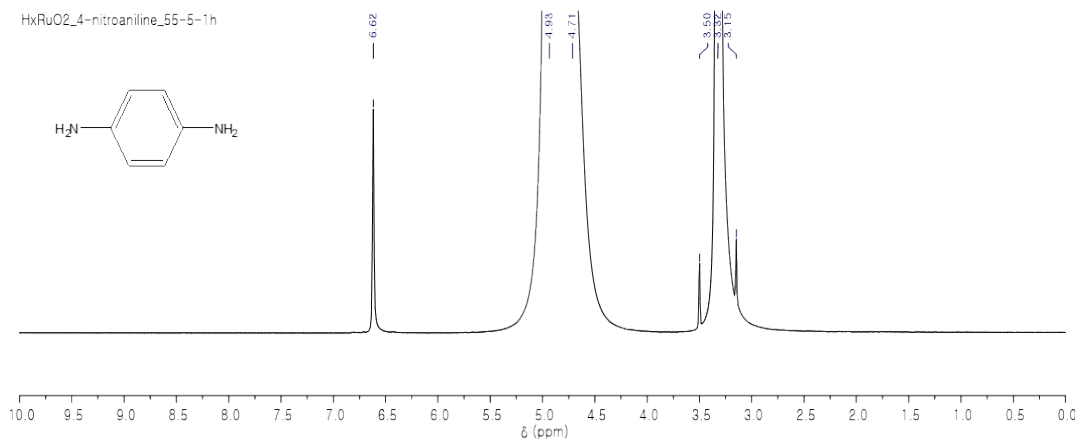
[Table S4, entry 2]



m-Aminophenol ^1H NMR (400 MHz, CD_3OD) δ 6.88 (q, 1H), δ 6.20 (q, 1H), δ 6.16 (d, 1H), δ 6.14 (s, 1H)

Retention time: 4.192 min (m-aminophenol)

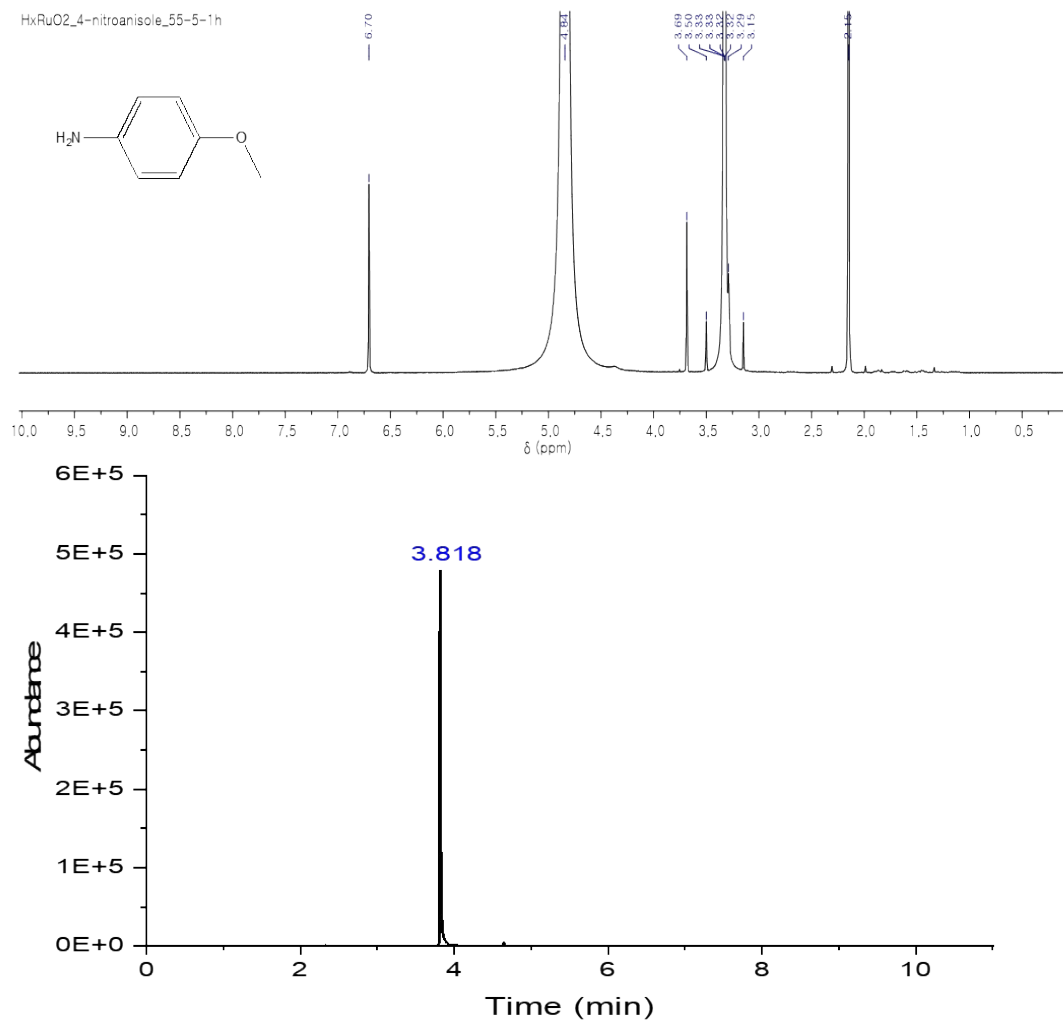
[Table S4, entry 3]



p-Aminoaniline ^1H NMR (400 MHz, CD_3OD) δ 6.62 (s, 4H)

Retention time: 4.053 min (p-aminoaniline)

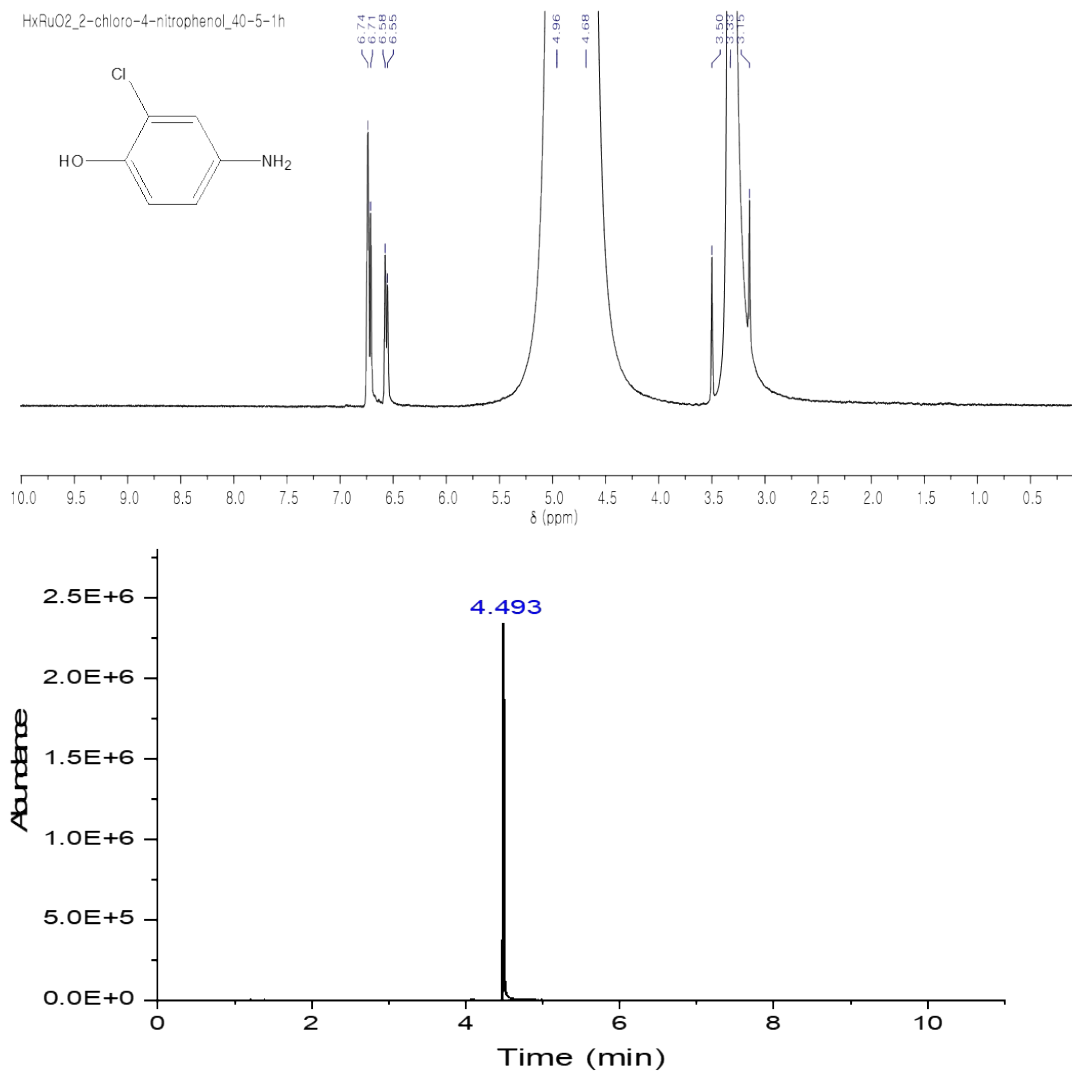
[Table S4, entry 4]



p-Aminoanisole ^1H NMR (400 MHz, CD_3OD) δ 6.72 (d, 2H), δ 6.70 (d, 2H), δ 3.70 (s, 3H)

Retention time: 3.818 min (p-aminoanisole)

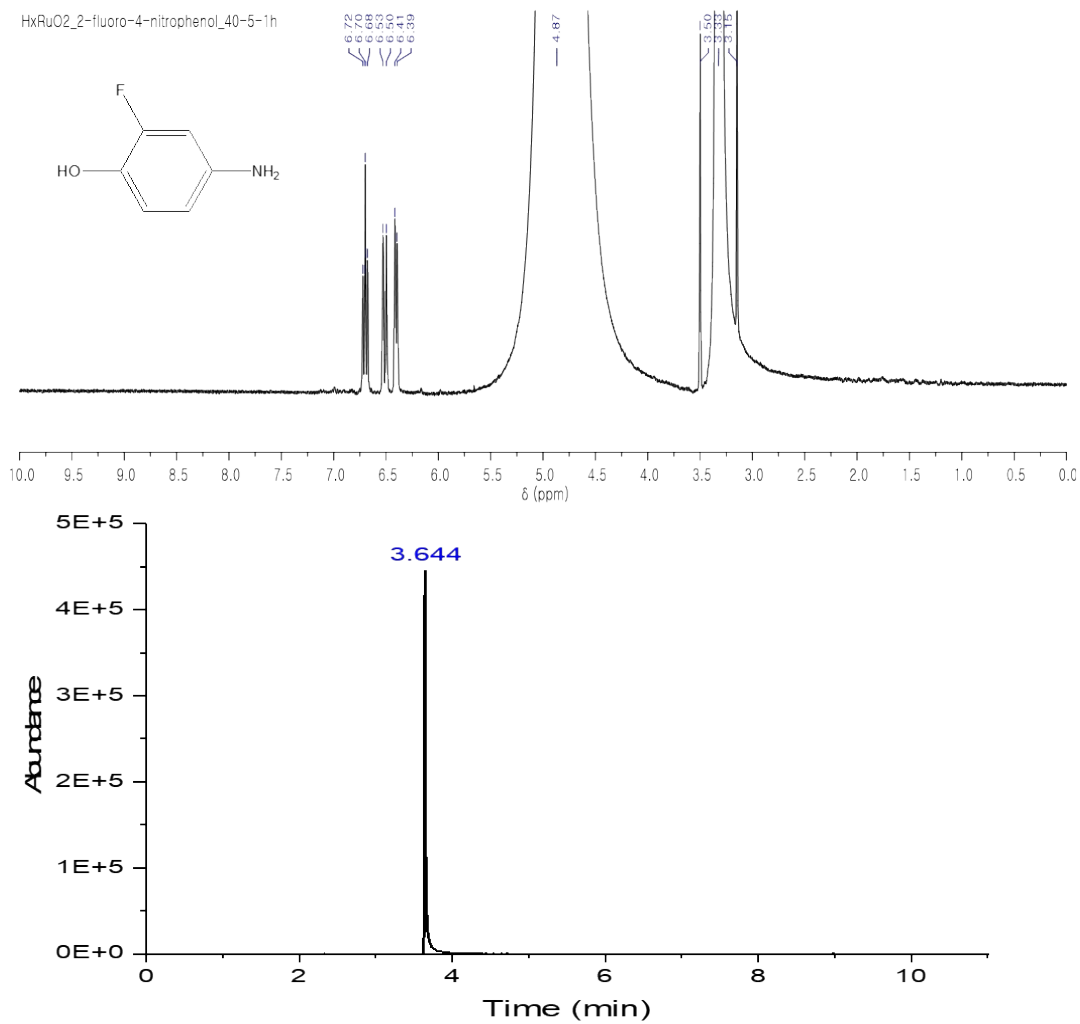
[Table S4, entry 5]



2-Chloro-4-aminophenol ^1H NMR (400 MHz, CD_3OD) δ 6.72 (s, 1H), δ 6.72 (d, 1H), δ 6.55 (d, 1H)

Retention time: 4.493 min (2-chloro-4-aminophenol)

[Table S4, entry 6]



2-Fluoro-4-aminophenol ^1H NMR (400 MHz, CD_3OD) δ 6.72 (d, 1H), δ 6.51 (s, 1H), δ 6.40 (d, 1H)

Retention time: 3.644 min (2-fluoro-4-aminophenol)